



Observations of neutral carbon in 29 high-z lensed dusty star-forming galaxies and the comparison of gas mass tracers

G. Gururajan, M. Bethermin, N. Sulzenauer, P. Theulé, J. S. Spilker, M. Aravena, S. C. Chapman, A. Gonzalez, T. R. Greve, D. Narayanan, et al.

► To cite this version:

G. Gururajan, M. Bethermin, N. Sulzenauer, P. Theulé, J. S. Spilker, et al.. Observations of neutral carbon in 29 high-z lensed dusty star-forming galaxies and the comparison of gas mass tracers. *Astronomy & Astrophysics* - A&A, 2023, 676, <10.1051/0004-6361/202346449>. <insu-04198350>

HAL Id: insu-04198350

<https://insu.hal.science/insu-04198350v1>

Submitted on 7 Sep 2023

HAL is a multi-disciplinary open access archive for the deposit and dissemination of scientific research documents, whether they are published or not. The documents may come from teaching and research institutions in France or abroad, or from public or private research centers.

L'archive ouverte pluridisciplinaire **HAL**, est destinée au dépôt et à la diffusion de documents scientifiques de niveau recherche, publiés ou non, émanant des établissements d'enseignement et de recherche français ou étrangers, des laboratoires publics ou privés.



Distributed under a Creative Commons CC BY 4.0 - Attribution - International License

Observations of neutral carbon in 29 high- z lensed dusty star-forming galaxies and the comparison of gas mass tracers

G. Gururajan^{1,2,3}, M. B'ethermin^{1,4}, N. Sulzenauer⁵, P. Theulé¹, J. S. Spilker⁶, M. Aravena⁷, S. C. Chapman^{8,9,10}, A. Gonzalez¹¹, T. R. Greve^{12,13}, D. Narayanan^{11,14,12}, C. Reuter¹⁵, J. D. Vieira^{15,16,17}, and A. Weiss⁵

¹ Aix-Marseille Univ., CNRS, CNES, LAM, Marseille, France

² University of Bologna – Department of Physics and Astronomy “Augusto Righi” (DIFA), Via Gobetti 93/2, 40129 Bologna, Italy
e-mail: gayathri.gururajan@unibo.it

³ INAF – Osservatorio di Astrofisica e Scienza dello Spazio, Via Gobetti 93/3, 40129 Bologna, Italy

⁴ Université de Strasbourg, CNRS, Observatoire astronomique de Strasbourg, UMR 7550, 67000 Strasbourg, France

⁵ Max-Planck-Institut für Radioastronomie, Auf dem Hügel 69, 53121 Bonn, Germany

⁶ Department of Physics and Astronomy and George P. and Cynthia Woods Mitchell Institute for Fundamental Physics and Astronomy, Texas A&M University, 4242 TAMU, College Station, TX 77843-4242, USA

⁷ Instituto de Estudios Astrofísicos, Facultad de Ingeniería y Ciencias, Universidad Diego Portales, Av. Ejército 441, Santiago, Chile

⁸ Department of Physics and Astronomy, University of British Columbia, 6225 Agricultural Road, Vancouver V6T 1Z1, Canada

⁹ National Research Council, Herzberg Astronomy and Astrophysics, 5071 West Saanich Road, Victoria V9E 2E7, Canada

¹⁰ Department of Physics and Atmospheric Science, Dalhousie University, 6310 Coburg Road, B3H 4R2 Halifax, Canada

¹¹ Department of Astronomy, University of Florida, 211 Bryant Space Sciences Center, Gainesville, FL 32611, USA

¹² Cosmic Dawn Center (DAWN), DTU-Space, Technical University of Denmark, Elektrovej 327, 2800 Kgs. Lyngby, Denmark

¹³ Department of Physics and Astronomy, University College London, Gower Place, WC1E 6BT London, UK

¹⁴ University of Florida Informatics Institute, 432 Newell Drive, CISE Bldg E251, Gainesville, FL 32611, USA

¹⁵ Department of Astronomy, University of Illinois at Urbana-Champaign, 1002 West Green St., Urbana, IL 61801, USA

¹⁶ Department of Physics, University of Illinois Urbana-Champaign, 1110 West Green Street, Urbana, IL 61801, USA

¹⁷ Center for AstroPhysical Surveys, National Center for Supercomputing Applications, Urbana, IL 61801, USA

Received 17 March 2023 / Accepted 5 June 2023

ABSTRACT

Context. The nature and evolution of high-redshift dusty star-forming galaxies (high- z DSFGs) remain open questions. Their massive gas reservoirs play an important role in driving the intense star formation rates hosted in these galaxies.

Aims. Our aim is to estimate the molecular gas content of high- z DSFGs by using various gas mass tracers, such as the [CI], CO, [CII] emission lines and the dust content. These tracers need to be well calibrated as they are all limited by uncertainties on factors such as α_{CO} , X_{CI} , $\alpha_{\text{[CII]}}$, and δ_{GDR} , thereby affecting the accurate determination of the gas mass. The main goal of our work is to check the consistency between the gas mass tracers and to cross-calibrate the uncertain factors.

Methods. We observed the two [CI] line transitions for 29 South Pole telescope Submillimeter Galaxies (SPT-SMGs) with the Atacama Large Millimeter/submillimeter Array–Atacama Compact Array (ALMA-ACA). Additionally, we also present new Atacama Pathfinder EXperiment (APEX) observations of [CII] line for nine of these galaxies. We combined our observations with the rich ancillary data of low- and mid- J CO lines, ancillary [CII] line, and dust mass estimations for these galaxies.

Results. We find a nearly linear relation between the infrared luminosity and [CI] luminosity if we fit the starbursts and main-sequence galaxies separately. We measure a median [CI]-derived excitation temperature of 34.5 ± 2.1 K. We probed the properties of the interstellar medium (ISM), such as density and radiation field intensity, using [CI] to mid- or high- J CO lines and the [CI]-to-infrared luminosity ratio, and find similar values to the SMG populations in the literature. Finally, the gas masses estimated from [CI], CO, dust, and [CII] do not exhibit any significant trend with the infrared luminosity or the dust temperature. We provide the various cross-calibrations between these tracers.

Conclusions. Our study confirms that [CI] is a suitable tracer of the molecular gas content, and shows an overall agreement between all the classical gas tracers used at high redshift. However, their absolute calibration, and thus the gas depletion timescale measurements, remain uncertain.

Key words. galaxies: high-redshift – galaxies: evolution – galaxies: ISM – galaxies: star formation – submillimeter: galaxies

1. Introduction

The formation and evolution of galaxies across cosmic time play an important role in understanding the evolution of the Universe. The cosmic star formation rate density (SFRD), when traced as a function of the redshift (z), shows a peak in star formation at $1 < z < 3$ (e.g., Madau et al. 1996; Le Floc'h et al. 2005; Hopkins & Beacom 2006; Madau & Dickinson 2014),

illustrating that more than half the stars we see today were already formed at $z \sim 1$ (Walter et al. 2011). At these redshifts, the most massive galaxies tend to be heavily dust obscured (e.g., Heinis et al. 2014; Fudamoto et al. 2020). These objects can host prodigious star formation rates (SFRs, $> 500 M_{\odot} \text{ yr}^{-1}$), and have a large contribution to the high- z SFRD (e.g., Madau & Dickinson 2014; Casey et al. 2014). Although they play a crucial role in our understanding of early

galaxy evolution, the nature and star formation mechanisms of such high- z dusty star-forming galaxies (DSFGs) remain unclear.

An important factor dictating the star formation rate and mechanism in a galaxy is its molecular gas content. The evolution of the molecular gas density with redshift, as shown by Decarli et al. (2020), among others, has a similar trend to that of the cosmic SFRD. Additionally, a rapid increase in the gas fraction ($f_{\text{gas}} \equiv M_{\text{gas}}/(M_{\text{gas}} + M_*)$) in galaxies with increasing redshifts (from $\sim 5\%$ at $z \sim 0$ to $\sim 50\%$ at $z \gtrsim 3$) is also shown by various surveys (e.g., Tacconi et al. 2010; Daddi et al. 2010a; Saintonge et al. 2013; Dessauges-Zavadsky et al. 2015, 2020; Béthermin et al. 2015). This could be driven by rapid accretion of cold gas from the cosmic web (e.g., Dekel et al. 2009; Kleiner et al. 2017; Kretschmer et al. 2020; Chun et al. 2020). The molecular gas content in a galaxy is mainly dominated by the H_2 molecule. As the H_2 molecule is not polar, it is mostly observable through vibrational transitions, which are currently inaccessible at high- z . Thus, we rely on other line emissions that can trace the H_2 content of a galaxy.

The carbon monoxide molecule (^{12}CO , hereafter CO) is one of the commonly used tracer of molecular H_2 content in a galaxy. The $J = 1-0$ transition of CO is assumed to be proportional to hydrogen column densities (n_{H_2} ; Solomon & Vanden Bout 2005; Bolatto et al. 2013). At high- z , particularly $z > 3$, the CO(1–0) line becomes harder to detect due to its low excitation temperature and the increasing influence of cosmic microwave background (CMB) emission at $z > 4$. We thus rely on mid- or high- J CO lines. Estimating the molecular gas mass from these lines requires assumptions of CO line excitation (Narayanan & Krumholz 2014; Tunnard & Greve 2016), and the CO-spectral line energy distribution for the various transitions have been modelled and constrained (e.g., Weiß et al. 2007; Harrington et al. 2021; Jarugula et al. 2021).

To estimate the molecular gas mass of a galaxy from the CO(1–0) luminosity, we need to assume a CO-to- H_2 conversion factor, α_{CO} . The value of α_{CO} is known to increase with decreasing metallicities as the size of the CO emission reduces (e.g., Maloney & Wolfire 1997; Wolfire et al. 2010; Krumholz et al. 2011; Shetty et al. 2011; Feldmann et al. 2012; Lagos et al. 2012; Narayanan et al. 2012). The value of α_{CO} was also shown to vary within the Milky Way (e.g., Oka et al. 1998; Strong et al. 2004; Sandstrom et al. 2013) and between normal star-forming galaxies (or disk-dominated systems) and starbursts (ultraluminous infrared galaxies, ULIRGs; e.g., Downes & Solomon 1998; Daddi et al. 2010b; Genzel et al. 2010). Furthermore, α_{CO} values can be affected by physical processes like mergers and radiation field intensity of the interstellar medium (ISM; e.g., Leroy et al. 2011; Magdis et al. 2011). Additionally, the destruction of CO molecules by cosmic rays in intensely star-forming environments can reduce their abundances, thereby underestimating the gas mass (Bisbas et al. 2015, 2017). Under typical ISM conditions, observations (e.g., Allen et al. 2012; Langer et al. 2014; Pineda et al. 2017) and theoretical works (e.g., Wolfire et al. 2010; Smith et al. 2014; Glover & Smith 2016) suggest that CO may miss nearly 30–70% of the total H_2 mass as the H_2 and CO may not be co-spatial in the ISM.

The molecular gas mass of a galaxy can also be estimated from its dust mass assuming a gas-to-dust ratio, δ_{GDR} (e.g., Magdis et al. 2011; Leroy et al. 2011; Eales et al. 2012; Scoville et al. 2014, 2016). The dust mass and dust temperature can be estimated by modelling far-infrared (FIR) and sub-millimetre emission of the spectral energy distribution (SED) of a galaxy. The value of δ_{GDR} is also sensitive to metallic-

ity, decreasing with increasing metallicity (e.g., Magdis et al. 2011; Leroy et al. 2011; Rémy-Ruyer et al. 2014; Capak et al. 2015; Popping & Péroux 2022; Popping et al. 2023). Therefore, assuming a single value of δ_{GDR} for all the galaxies across a wide range of redshifts might not be accurate. Additionally, δ_{GDR} is also dependent on dust grain properties and the models describing the creation or destruction of dust (Bolatto et al. 2013).

In recent years, the ionised carbon fine structure emission line [CII] at $158\mu\text{m}$ has been advocated as an estimator of molecular gas mass (e.g., Hughes et al. 2017; Zanella et al. 2018; Dessauges-Zavadsky et al. 2020; Vizgan et al. 2022). [CII] emission arises from multiple phases of the ISM, such as the photodissociation regions (PDRs); the atomic, molecular, and diffuse ionised regions (e.g., Stacey et al. 1991; Kaufman et al. 1999; Sargsyan et al. 2012; Rigopoulou et al. 2014; Croxall et al. 2017). This makes it difficult to disentangle the contributions of these various regions to the [CII] emission. However, $\sim 75\%$ of [CII] emission is thought to arise from the PDRs (Pineda et al. 2014; Cormier et al. 2015; Díaz-Santos et al. 2017); most of which arise in the molecular phase (e.g., Pineda et al. 2013; Velusamy & Langer 2014). This has also been found in simulations of high- z galaxies (e.g., Vallini et al. 2015; Popping et al. 2019). Zanella et al. (2018) describe an empirical relation between [CII] luminosity and molecular gas mass for a sample of main-sequence galaxies and ULIRGs, with a [CII]-to- H_2 conversion factor, $\alpha_{[\text{CII}]}$. They found that $\alpha_{[\text{CII}]}$ does not seem to vary with metallicity or the mode of star formation.

An alternative and promising tracer of the molecular gas content is the atomic carbon fine structure lines. The two transitions $\text{C}_1(^3\text{P}_2-^3\text{P}_1)$ and $\text{C}_1(^3\text{P}_1-^3\text{P}_0)$, hereafter the [CI](2–1) and [CI](1–0) lines, respectively, can also be used to estimate the gas content of a galaxy (e.g., Keene et al. 1985; Papadopoulos et al. 2004; Papadopoulos & Greve 2004). The [CI] emission in the ISM of a galaxy was thought to arise only in a small region of the PDR, between the CO and [CII] (Langer 1976; Tielens & Hollenbach 1985). Theoretical works (Tomassetti et al. 2014) and the detection of [CI] in the Galactic molecular clouds along with CO, have suggested that [CI] emission is more extended in the ISM (Keene et al. 1985; Ojha et al. 2001), thereby making it a candidate for tracing the molecular gas content. Studies have also shown that [CI] arises from the same volume as CO(1–0) (e.g., Plume et al. 1999; Ikeda et al. 2002; Schneider et al. 2003; Pérez-Beaupuits et al. 2015). The accuracy of the [CI](1–0) line as a tracer of molecular gas content has thus been advocated by many studies (e.g., Papadopoulos et al. 2004; Weiß et al. 2003; Dunne et al. 2021). Additionally, it is optically thin for the bulk of the H_2 gas (Pérez-Beaupuits et al. 2015) facilitating its detection in intense starbursts, and the excitation temperature of [CI] is sufficiently low ($\sim 24\text{ K}$, Dunne et al. 2022), thereby tracing cold gas effectively.

In order to estimate the molecular gas mass from the [CI](1–0) observations, it is necessary to assume a [CI] abundance – X_{CI} . It can also be affected by factors such as metallicity and densities (Bisbas et al. 2021; Heintz & Watson 2020), but it is less sensitive to metallicity than α_{CO} (e.g., Leroy et al. 2011; Genzel et al. 2012; Schrubba et al. 2012; Shi et al. 2015, 2016; Heintz & Watson 2020; Bisbas et al. 2021). Similarly to CO, the [CI] excitation must also be known to accurately derive the gas mass. The [CI] excitation factor or partition function, Q_{10} , can be constrained if the excitation temperature of [CI] in the ISM is known.

Owing to its relatively simple two-level excitation, and assuming local thermodynamical equilibrium (LTE) conditions, the excitation temperature of [CI] in the ISM can be estimated as a function of the ratio of the two [CI] line luminosities (e.g., Stutzki et al. 1997; Weiß et al. 2003; Papadopoulos et al. 2004; Walter et al. 2011). The excitation temperature of the ISM can also be compared with the dust temperature as they are expected to be linear under LTE, assuming an effective gas to dust coupling (e.g., Carilli & Walter 2013; da Cunha et al. 2013; Valentino et al. 2020). Other parameters, such as the radiation field intensity and the density of the ISM, can also be constrained using various line ratios. Mid- and high- J CO lines are expected to arise from warm and dense ISM; when compared to an extended gas tracer such as [CI], the line ratio could be a proxy to the density of the ISM (e.g., Alaghband-Zadeh et al. 2013; Yang et al. 2017; Andreani et al. 2018; Valentino et al. 2018, 2020).

In this paper we explore the properties of the [CI] line and its ability as a molecular gas tracer using a sample of 29 lensed DSFGs from the South Pole telescope Submillimeter Galaxy (SPT-SMG) sample. Gravitational lensing can boost the apparent flux, thereby making these DSFGs bright enough to detect, and allowing us to build a statistical sample of [CI] detection at high- z . With the data in hand, we study the relation between the [CI] line luminosity and the infrared luminosity. We compare the [CI] excitation temperature with the dust temperature. We use the combination of [CI] and other observables to constrain ISM properties of our sample. Finally, we compare [CI] to other molecular gas tracers such as CO, [CII], and dust to cross-calibrate the unknown factors, such as, X_{CI} , α_{CO} , $\alpha_{\text{[CII]}}$, and δ_{GDR} , in these tracers.

The structure of this paper is as follows. The sample selection, the ALMA/ACA observations and the APEX-[CII] observations are presented in Sect. 2. In Sect. 3 we describe the data processing, the imaging, and the flux extraction for our sample. We analyse the properties of the [CI] line in Sect. 4, where we probe the relation between the infrared and [CI] luminosities (Sect. 4.1), the [CI] excitation temperature (Sect. 4.2), and the properties of the ISM as traced by the line and line-to-continuum ratios (Sect. 4.3). We then compare the gas mass estimated with the [CI] line with other tracers such as the CO, dust continuum, and [CII] emission line, and cross-calibrate these tracers in Sect. 5.1. In Sect. 6.2 we discuss the results of our cross-calibration of the various gas mass tracers and probe the gas depletion timescales for our sample as a function of their redshifts (Sect. 6.3). We conclude in Sect. 7.

Throughout this paper, we adopt a Λ CDM cosmology with $\Omega_m = 0.3$, $\Omega_\Lambda = 0.7$, and $H_0 = 70 \text{ km s}^{-1} \text{ Mpc}^{-1}$ and a Chabrier (2003) initial mass function (IMF).

2. Sample and ALMA observations

2.1. Sample selection

We built a statistical sample of 30 galaxies targeting both the [CI] lines from the SPT-SMG sample (Vieira et al. 2013; Weiß et al. 2013; Strandet et al. 2016; Reuter et al. 2020). These galaxies are in the ideal redshift range ($1.87 < z < 4.8$) to allow the observations of both the [CI] transitions with ALMA (with the bands available in the cycle and in frequencies unaffected by atmospheric absorption). For this sample, 21 ancillary [CI](1–0) observations exist from the observations presented in Bothwell et al. (2017) and Reuter et al. (2020). In this work, we present 39 observations of [CI] lines (30 observations of

the [CI](2–1) line and 9 observations of the [CI](1–0) line) with ALMA-ACA (PI: Bethermin, 2019.1.00297.S) to build a complete sample with the ancillary data for these 30 galaxies. We also present the APEX-[CII] observations for nine of these galaxies (M-090.F-0016-2012, M-093.F-0012-2014, M-095.F-0028-2015, M-097.F-0019-2016). Nine additional galaxies have ancillary [CII] observations from Gullberg et al. (2015). The ACA observations are described in Sect. 2.2 and the APEX-[CII] observations are described in Sect. 2.3. For this sample, ancillary low- J CO observations from Aravena et al. (2016) and mid- J CO observations from Reuter et al. (2020) are also available. Unfortunately, most of these sources lack an estimate of the stellar masses as the near-infrared bright foreground lens usually outshines the DSFG. However, for six SPT-SMGs, the stellar masses were estimated based on IRAC photometry, but remain uncertain (Ma et al. 2015). These sources were found above the main sequence of star-forming galaxies, but because of the uncertainties it is not fully clear if they are starbursts or just on the upper envelop of the relation.

For the [CI](1–0) transition, the observed frequency was required to be higher than 84 GHz ($z < 4.8$) to be within the observation limit of band 3 and not in the range 116–125 GHz ($2.9 < z < 3.2$), as it corresponds to the gap between band 3 and band 4. Additionally, we excluded the frequency range 175–190 GHz ($3.2 < z < 3.6$) for [CI](2–1) as it can fall in a strong atmospheric water absorption feature in band 5, and thus would require a very long integration with excellent weather for a detection, which could lead to bad-quality data. Thus, we present 21 [CI](2–1) observations in $3.6 < z < 4.8$ for which there is existing [CI](1–0) observations from the ancillary data and ten galaxies at $z < 2.9$ for which both the [CI] lines can be observed.

Together with the [CI](2–1) line, we observed simultaneously the CO(7–6) line since they are close in frequency. For three of our sources, we also have the CO(4–3) line imaged on the lower sideband of [CI](1–0) observational set-up. All these galaxies are strongly gravitationally lensed, and 18 of them have detailed lens modelling presented in Spilker et al. (2016). For the sources without lens modelling, we assumed a median magnification of 5.5 (Reuter et al. 2020). This median value of magnification was adopted based on the available lens models for a sample of 39 SPT-SMGs presented in Spilker et al. (2016). As the sources presented in Spilker et al. (2016) for lens modelling were drawn at random from a larger sample of SPT-SMGs, the median value of magnification adopted is a reasonable assumption. Our sample is presented in Table 1.

The initial ACA proposal consisted of 39 observations; one of our sources, SPT0452-52, was not detected in either [CI](2–1) or [CI](1–0). This source had not been detected clearly in the earlier band 3 observations presented in Reuter et al. (2020), and hence we suspect an ambiguous redshift to be the cause of the non-detection. We thus chose to discard this source from our analysis. Hence, we proceeded with a final sample of 29 galaxies with both [CI] transitions; 18 of the 29 galaxies also have [CII] line observations using APEX (see Sect. 2.3) and 5 galaxies are with [CI](2–1) from the APEX observations.

2.2. ALMA/ACA observations

Our target sources were observed with the Atacama compact array (ACA) of ALMA. We do not spatially resolve our sources and thus ACA is perfect as it is always in a very compact configuration contrary to the 12 m configuration which changes. Owing to the low surface density of the SPT sources, we cannot share

Table 1. ALMA/ACA observation details of our sample.

Source	Target line	Observed frequency (GHz)	Observation date(s)	Time on source (min)	PWV (mm)	σ_{channel} (mJy)	Resolution “x”
SPT0002-52	[CI](1–0)	146.87	29/10/2019	17	0.5	2.4	12.6×8.8
	[CI](2–1)	241.52	08/10/2019	8	0.9	4.4	7.3×4.9
SPT0020-51	[CI](2–1)	157.98	13/10/2019	18	1.8	2.8	11.1×7.6
SPT0113-46	[CI](2–1)	154.66	13/10/2019	49	1.6	1.7	11.3×7.4
SPT0125-50	[CI](2–1)	163.27	09/11/2019	24	1.4	2.4	11.5×6.9
SPT0136-63	[CI](2–1)	152.73	15/11/2019	29	2.0	2.0	12.5×7.7
SPT0150-59 (*)	[CI](1–0)	129.93	03/11/2019	28	4.8	2.4	12.8×10.2
	[CI](2–1)	213.66	12/10/2019	20	2.1	3.7	9.1×5.6
SPT0155-62	[CI](2–1)	151.31	01/11/2019	19	2.0	3.4	11.1×8.8
SPT0319-47	[CI](2–1)	146.89	31/10/2019	17	3.4	3.6	10.4×8.9
SPT0345-47	[CI](2–1)	152.82	02/11/2019	17	0.01	3.3	10.3×8.5
SPT0418-47	[CI](2–1)	154.9	31/10/2019	17	3.5	3.7	10.1×8.6
SPT0441-46	[CI](2–1)	147.77	31/10/2019	17	3.4	3.1	10.6×8.7
SPT0459-59	[CI](2–1)	139.57	02/11/2019	24	3.2	2.5	12.0×10.1
SPT0512-59	[CI](1–0)	152.23	31/10/2019	18	3.5	3.1	10.2×9.8
	[CI](2–1)	250.34	13/11/2019	21	1.6	6.0	6.5×5.6
SPT0544-40	[CI](2–1)	153.6	13/10/2019	17	0.01	3.6	12.6×7.6
SPT0551-48 (*)	[CI](1–0)	137.36	01/10/2019	17	3.0	2.4	13.4×8.2
	[CI](2–1)	225.88	03/10/2019	18	1.4	3.4	9.0×4.9
SPT0552-42	[CI](2–1)	148.86	01/10/2019	38	2.6	2.0	11.9×8.0
SPT0604-64	[CI](1–0)	141.38	01/10/2019	19	2.9	2.9	12.8×9.8
	[CI](2–1)	232.5	10/11/2019	21	1.6	4.2	7.3×6.0
SPT2037-65	[CI](2–1)	161.87	01/10/2019	17	1.6	3.0	9.5×8.6
SPT2048-55 (a,*)	[CI](2–1)	159.01	13/10/2019	29	3.0	1.6	11.6×7.6
	[CI](2–1)		13/10/2019	29	2.8		
	[CI](2–1)		17/11/2019	29	3.4		
SPT2103-60	[CI](2–1)	148.89	02/10/2019	18	2.5	3.4	12.2×9.6
SPT2132-58 (*)	[CI](2–1)	140.32	12/10/2019	21	2.1	1.8	12.9×9.0
SPT2134-50 (*)	[CI](1–0)	130.2	02/11/2019	26	5.4	3.1	12.9×10.2
	[CI](2–1)	214.11	04/10/2019	18	1.6	3.4	7.7×5.6
SPT2146-55	[CI](2–1)	145.38	13/10/2019	21	2.0	1.9	11.8×8.7
SPT2147-50	[CI](2–1)	170.03	01/10/2019	28	1.4	2.3	9.6×7.0
SPT2311-54	[CI](2–1)	153.28	30/10/2019	19	0.8	2.8	10.3×8.9
SPT2335-53	[CI](2–1)	140.58	13/10/2019	26	1.8	1.6	12.1×8.2
SPT2349-50	[CI](1–0)	126.94	31/10/2019	29	3.9	2.6	13.2×9.5
	[CI](2–1)	208.75	29/10/2019	20	0.7	3.8	9.5×5.9
SPT2349-56 (*,†)	[CI](1–0)	152.59	30/10/2019	41	3.7	1.7	11.7×8.2
SPT2354-58	[CI](1–0)	171.66	23/10/2019	27	1.1	1.9	9.6×7.4
	[CI](2–1)	282.3	11/10/2019	35	1.1	3.1	5.8×4.1

Notes. Some of our sources were observed for both [CI] transitions, and thus have multiple observation dates. The precipitable water vapour (PWV) during the observation is given in mm. The channel sensitivity is the mean computed over every channel for a corresponding channel width of 0.031 GHz. The line resolution of the source is given in terms of the major axis \times minor axis. ^(†)Protocluster candidate ^(*)The sources for which the sensitivity is computed in a channel width of 0.063 GHz. ^(a)The source was observed on multiple dates and the different datasets were concatenated to proceed with the analysis. The channel sensitivity, width, and resolution are for the concatenated dataset.

a calibrator since sources sharing a similar correlator set-up are too distant from each other. Hence using the 12 m array would result in a shorter on-source observation time than the calibration. This would be an inefficient use of the telescope time and the observations would be mainly calibrations and overheads. We thus chose to observe in ACA configuration with median on-source observation time of 21.2 min with a comparatively short calibration time. This also required only between 10 and 12 of the 7 m antennas, and was a better use of telescope time.

To maximise the sensitivity of the integrated [CI] and CO fluxes, we required the entire source flux to be well-encompassed within a single synthesised beam. The median angular resolution

reached by ACA for our sample is 8.85 arcsec, while the sources are more compact than ~ 2 arcsec.

For all our targets we used four spectral windows for every observation to secure the measurements of lines and the continuum. This also ensures maximal coverage of both the upper and the lower side bands. For the [CI](2–1) lines, we used one spectral window in frequency division mode (FDM) with a spectral resolution of 7.813 MHz. This spectral window is centred on the [CI](2–1) observed frequency. As the observer-frame frequency separation between [CI](2–1) and CO(7–6) is <1 GHz for our sample, they could be imaged in the same spectral window. We also placed a second spectral window (with the same resolution)

adjacent to it, in order to target any possible tails in the CO(7–6) emission. To measure the continuum emission, we used the other two spectral windows in time division mode (TDM) with a coarser resolution of 31.25 MHz.

To observe the [CII](1–0) line, we placed one spectral window (7.813 MHz resolution), centred at its observed frequency. The other three spectral windows were used to measure the continuum emission. For four of our sources ($1.86 < z < 2.35$), we could also observe CO(4–3) by simultaneously shifting approximately one-fourth of the width of the [CII](1–0) window to higher frequencies. This did not affect the [CII](1–0) measurements as the line width ($< 1000 \text{ km s}^{-1}$) is lower than the velocity range of the spectral window ($\sim 3500 \text{ km s}^{-1}$).

We aimed to achieve a sensitivity of 5σ when integrated over the full line width ($\sim 400 \text{ km s}^{-1}$) for both lines for our sample. The target sensitivities for the [CII](1–0) line were estimated from their IR luminosities (L_{IR}) assuming an $L_{\text{[CII](1-0)}}/L_{\text{IR}}$ ratio of $10^{-2.8}$. The L_{IR} measurements are well-constrained from the existing *Herschel* and LABOCA observations (Reuter et al. 2020). For the [CII](2–1) line, we assumed a [CII](2–1)/[CII](1–0) flux ratio of 1.1 from the best-fit solution of the PDR modelling of Bothwell et al. (2017).

The on-source integration time is significantly shorter than the calibration time, for a few bright sources, when the required sensitivity is $> 1.6 \text{ mJy beam}^{-1} \text{ RMS}$ in 400 km s^{-1} . We thus fixed the RMS goal to a maximum value of $1.6 \text{ mJy beam}^{-1}$, as a higher signal-to-noise ratio could be a poor use of telescope time especially if the line is fainter than predicted and overhead dominated observations are not ideal. With the same sensitivity, the CO(7–6) line should also be detected as it is generally brighter than [CII](2–1). We present the observation details of our sample in Table 1. The sensitivity and resolution correspond to the achieved values and their estimation is described in Sect. 3.1.

2.3. APEX [CII] observations

APEX [CII] observations were carried out using the First Light APEX Submillimetre Heterodyne receiver (FLASH; Heyminck et al. 2006). Ten sources at $4.0 < z < 4.8$ ($\nu_{\text{obs}} = 327\text{--}388 \text{ GHz}$) were observed in the 345 GHz channel between 2014 July and 2017 September, during Max Planck time. All observations were done in good weather conditions with an average precipitable water vapour $< 1.1 \text{ mm}$, yielding typical system temperatures of 230 K. The beam sizes/antenna gains are $18.0 \text{ arcsec}/40 \text{ Jy K}^{-1}$ and $15.0 \text{ arcsec}/42 \text{ Jy}^{-1}$ respectively for the lowest and highest observed frequencies of the [CII] line. The beam size is much larger than the observed Einstein radii of these sources, and thus they are unresolved (Spilker et al. 2016). The 92 h of observations were done in wobbler switching mode, with switching frequency of 1.5 Hz and a wobbler throw of 50 arcsec in azimuth. Pointing was checked frequently and was found to be stable to within 2.5 arcsec. Calibration was done every $\sim 10 \text{ min}$ using the standard hot–cold load absorber measurements. The data were recorded with the MPIfR fast Fourier transform spectrometers (FFTS, Klein et al. 2006) providing $4 \times 2.5 \text{ GHz}$ of bandwidth to cover the full 4 GHz bandwidth in each of the upper and lower sidebands of the sideband-separating FLASH receiver.

The data were processed with the Continuum and Line Analysis Single-dish Software (CLASS). We visually inspected the individual scans and omitted scans with unstable baselines, resulting in $< 10\%$ loss. We subtracted linear baselines from the individual spectra in each of the two FFTS units, and regridded to a velocity resolution of $\sim 90 \text{ km s}^{-1}$ in the averaged spectra.

On-source integration times were between 2 and 15 h. The line intensities are summarised in Table 2.

2.4. APEX [CII](2–1) sample and observations

In addition to our ACA sample, we also include a sample of nine DSFGs for which we targeted the [CII](2–1) lines with the APEX/SEPIA instrument (PIs: Bèthermin and Strandet, project number: 097.A-0973). Six of the sources had tentative detections in the [CII](2–1) and/or CO(7–6) lines. For SPT0551-50 there was an ambiguity in the redshift, and thus the APEX set-up did not cover the [CII](2–1) observation window. The redshift was constrained with the updated spectral scans presented in Reuter et al. (2020). We used the CLASS package of the GILDAS software¹ to reduce the data, and we used an automatic procedure described in Zhang et al. (in prep.) to assess the data quality and flag the bad data and baselines. The APEX/SEPIA spectra are presented in Fig. B.1.

Using an antenna gain conversion factor of 38 Jy K^{-1} , we obtained the APEX intensities. We then defined a narrow integration window around the line peak and summed the intensities in this manually defined range. We estimated the noise by computing the standard deviation on the line-free channels multiplied by \sqrt{N} , where N is the number of channels used to estimate the line flux.

3. Data analysis

3.1. Line imaging and performance

Initial calibrations of the data are done by the observatory using the standard ALMA pipeline based on the Common Astronomy Software Applications (CASA, McMullin et al. 2007). We then image our data using the tcLEAN routine in CASA. All our sources are unresolved and thus we use a natural weighting function to optimise the S/N of our flux measurements.

We make a first CLEANing using the *cube* mode of tcLEAN. From this first image, we can estimate the rms noise (σ_{rms}) to determine the cleaning threshold. Additionally, we visualise the data to choose the relevant continuum model to use for its subtraction (constant or first-degree). We also check whether the lines are clearly detected or if the data needs further re-binning. We then visually estimate the frequencies and the width of the line, which is useful while subtracting the continuum emission.

The next step is to obtain the line cubes, free of any continuum emission. For this, we use the *uvcontsub* task of CASA. We can define the spectral windows and the frequency range containing our line emission, and the continuum model (constant or first-degree). This task then subtracts the continuum emission in the u – v plane of our data cube and returns a continuum-free data cube.

Finally, we re-image the continuum-free line cubes with a cleaning threshold of $3\sigma_{\text{noise}}$, and re-bin the data by a factor of 4 to further improve the S/N of each bin in our line images. From these line datacubes, we can estimate the noise level at the phase-centre by computing the standard deviation at every channel of the non-primary beam corrected line cubes, after masking the source. In Table 1, the mean sensitivity per channel (σ_{channel}) is given for all our observations. The sensitivity for our sources varies from 1.6–6.0 mJy, with an average sensitivity of 2.9 mJy in a channel width of 0.031 GHz.

¹ <https://www.iram.fr/IRAMFR/GILDAS/>

Table 2. [CI](1–0), [CI](2–1), CO(7–6), and [CII] line fluxes estimated for our sample.

Source	z	RA (J2000)	Dec (J2000)	[CI](1–0) (Jy km s ^{−1})	[CI](2–1) (Jy km s ^{−1})	CO(7–6) (Jy km s ^{−1})	[CII] (Jy km s ^{−1})
SPT0002-52	2.351	0:02:23.76	−52:31:52.7	3.85 ± 0.45	8.71 ± 0.98	14.87 ± 0.84	
SPT0020-51	4.123	0:20:23.58	−51:46:36.4	1.98 ± 0.47 ^(b)	6.32 ± 0.89	8.12 ± 1.08	
SPT0113-46	4.233	1:13:09.01	−46:17:56.1	3.36 ± 0.68 ^(a)	4.26 ± 0.67	4.48 ± 0.73	82.1 ± 13.3 ^(c)
SPT0125-50	3.957	1:25:48.45	−50:38:21.0	2.37 ± 0.53 ^(a)	4.85 ± 0.46	7.29 ± 0.6	<326.5
SPT0136-63	4.299	1:36:50.28	−63:07:26.7	1.14 ± 0.62 ^(b)	<4.98	4.62 ± 0.92	40.8 ± 6.3
SPT0150-59	2.788	1:50:09.26	−59:23:57.1	3.29 ± 0.84	6.76 ± 0.81	12.03 ± 1.25	
SPT0155-62	4.349	1:55:47.75	−62:50:50.0	5.06 ± 0.58 ^(b)	7.08 ± 0.85	11.61 ± 1.12	
SPT0319-47	4.51	3:19:31.88	−47:24:33.6	<8.4 ^(b)	3.24 ± 0.63	4.00 ± 0.88	32.1 ± 7.6
SPT0345-47	4.296	3:45:10.77	−47:25:39.5	<1.03 ^(a)	<4.96	12.16 ± 1.05	44.6 ± 9.0 ^(c)
SPT0418-47	4.225	4:18:39.67	−47:51:52.5	2.46 ± 0.61 ^(a)	3.57 ± 0.68	7.29 ± 0.87	116.0 ± 12.1 ^(c)
SPT0441-46	4.477	4:41:44.08	−46:05:25.6	<2.22 ^(a)	4.01 ± 1.04	6.57 ± 0.88	37.4 ± 6.6 ^(c)
SPT0459-59	4.799	4:59:12.34	−59:42:20.3	2.43 ± 0.7 ^(a)	3.77 ± 0.89	5.74 ± 0.93	<57.5
SPT0512-59	2.233	5:12:57.98	−59:35:42.0	9.55 ± 0.9	15.73 ± 1.31	14.26 ± 1.15	
SPT0544-40	4.269	5:44:01.12	−40:36:31.2	<7.78 ^(b)	4.47 ± 0.99	5.16 ± 0.93	41.8 ± 8.6
SPT0551-48	2.583	5:51:54.65	−48:25:01.8	7.03 ± 1.09	12.08 ± 0.62	34.09 ± 0.65	
SPT0552-42	4.437	5:52:26.52	−42:44:12.7	<4.68 ^(b)	3.31 ± 0.61	2.53 ± 0.57	39.6 ± 5.4
SPT0604-64	2.481	6:04:57.57	−64:47:22.0	9.80 ± 0.5	13.03 ± 0.84	18.11 ± 0.86	
SPT2037-65	3.998	20:37:31.98	−65:13:16.8	<4.44 ^(b)	5.23 ± 0.87	7.53 ± 0.62	
SPT2048-55	4.09	20:48:22.87	−55:20:41.3	1.39 ± 0.44 ^(b)	2.49 ± 0.66	1.68 ± 0.47	<68.5
SPT2103-60	4.436	21:03:30.90	−60:32:39.9	3.07 ± 0.76 ^(a)	4.59 ± 1.23	5.57 ± 0.89	52.0 ± 17.2 ^(c)
SPT2132-58	4.768	21:32:43.23	−58:02:46.4	<0.87 ^(a)	2.56 ± 0.76	5.27 ± 0.86	43.4 ± 13.4 ^(c)
SPT2134-50	2.78	21:34:03.34	−50:13:25.2	5.70 ± 1.15	8.24 ± 1.03	20.60 ± 1.19	
SPT2146-55	4.567	21:46:54.02	−55:07:54.7	2.73 ± 0.71 ^(a)	3.52 ± 0.79	4.86 ± 1.04	33.4 ± 7.1 ^(c)
SPT2147-50	3.76	21:47:19.05	−50:35:53.5	2.01 ± 0.6 ^(a)	4.90 ± 0.7	6.37 ± 0.94	101.9 ± 14.3 ^(c)
SPT2311-54	4.28	23:11:23.97	−54:50:30.1	<7.56 ^(b)	8.36 ± 1.22	4.72 ± 0.61	38.0 ± 3.8 ^(c)
SPT2335-53	4.757	23:35:13.96	−53:24:21.0	<2.34 ^(b)	<3.08	1.75 ± 0.49	12.4 ± 3.3
SPT2349-50	2.877	23:49:42.20	−50:53:30.9	3.58 ± 0.68	4.14 ± 0.63	3.74 ± 0.68	
SPT2349-56	4.304	23:49:42.78	−56:38:23.2	<2.94 ^(b)	<2.44	<2.03	79.5 ± 11.5
SPT2354-58	1.867	23:54:34.31	−58:15:08.3	5.06 ± 0.56	11.62 ± 0.75	23.58 ± 0.82	

Notes. The redshift (z), the right ascension (RA), and declination (dec) are tabulated along with the [CI](1–0), [CI](2–1), CO(7–6), and [CII] fluxes. The fluxes presented in this table are not corrected for magnification. The errors given on the fluxes are 1σ errorbars, and the upper limits are 3σ . ^(a) Ancillary [CI](1–0) fluxes from [Bothwell et al. \(2017\)](#). ^(b) Ancillary [CI](1–0) fluxes from [Reuter et al. \(2020\)](#). ^(c) Ancillary [CII] fluxes from [Gullberg et al. \(2015\)](#).

3.2. Spectrum extraction and flux estimation

We imaged the continuum emission of our sources by selecting the line-free spectral windows and using the multi-frequency synthesis mode (MFS; [Conway et al. 1990](#)) of *tcLEAN* of CASA. This generated the continuum map of our sources. All our sources are gravitationally lensed and the lens models are presented in [Spilker et al. \(2016\)](#). Our sources are unresolved and well encompassed in the beam. We verified that the continuum position is in agreement with the source coordinates presented in [Reuter et al. \(2020\)](#). Assuming that the continuum and the line emission are co-spatial, we can extract the spectra at the position of the peak of continuum emission. We thus extracted the spectrum from the line cubes at this exact position of the continuum emission. The [CI](1–0) and [CI](2–1) spectra of our sample are presented in Figs. 1 and 2, respectively.

From the spectra we were able to visually estimate the integration window of the line emission for our sources with sufficient signal of the line. This frequency range was then used as the integration range to obtain the integrated fluxes for each of the lines. In Fig. 2, the blue shaded region represents the [CI](2–1) integration window, the red shaded region

represents the CO(7–6) integration window. The violet shaded region in Fig. 1 represents the [CI](1–0) integration window. For four of our sources, SPT0136-63, SPT0345-47, SPT2335-53, and SPT2349-56, the [CI](2–1) line is not visually detected (i.e. the signal is not sufficient), and thus we used a width of 400 km s^{-1} (approximately the median width of the [CI](2–1) line of our sample) as a line integration width to estimate the upper limits of the line fluxes. The [CI](2–1) line of two of our sources, SPT0150-59 and SPT0155-62, are blended with the CO(7–6) emission. In order to properly estimate the fluxes in this scenario, we estimated the width of the line by fitting the spectra using a two-Gaussian profile and estimating the width of each component (see Sect. C).

To estimate the integrated flux of these lines, we constructed a moment-0 map using the *immoments* function of CASA. The integration windows for these lines are represented in Figs. 1 and 2. For the two sources with blended [CI](2–1) and CO(7–6) emission, we used the width estimated from the Gaussian fitting as the integration range in the moment-0 maps. From these moment-0 maps, we measured the integrated flux at the continuum source position. Since the source is unresolved, the flux was well contained in a single synthesised beam.

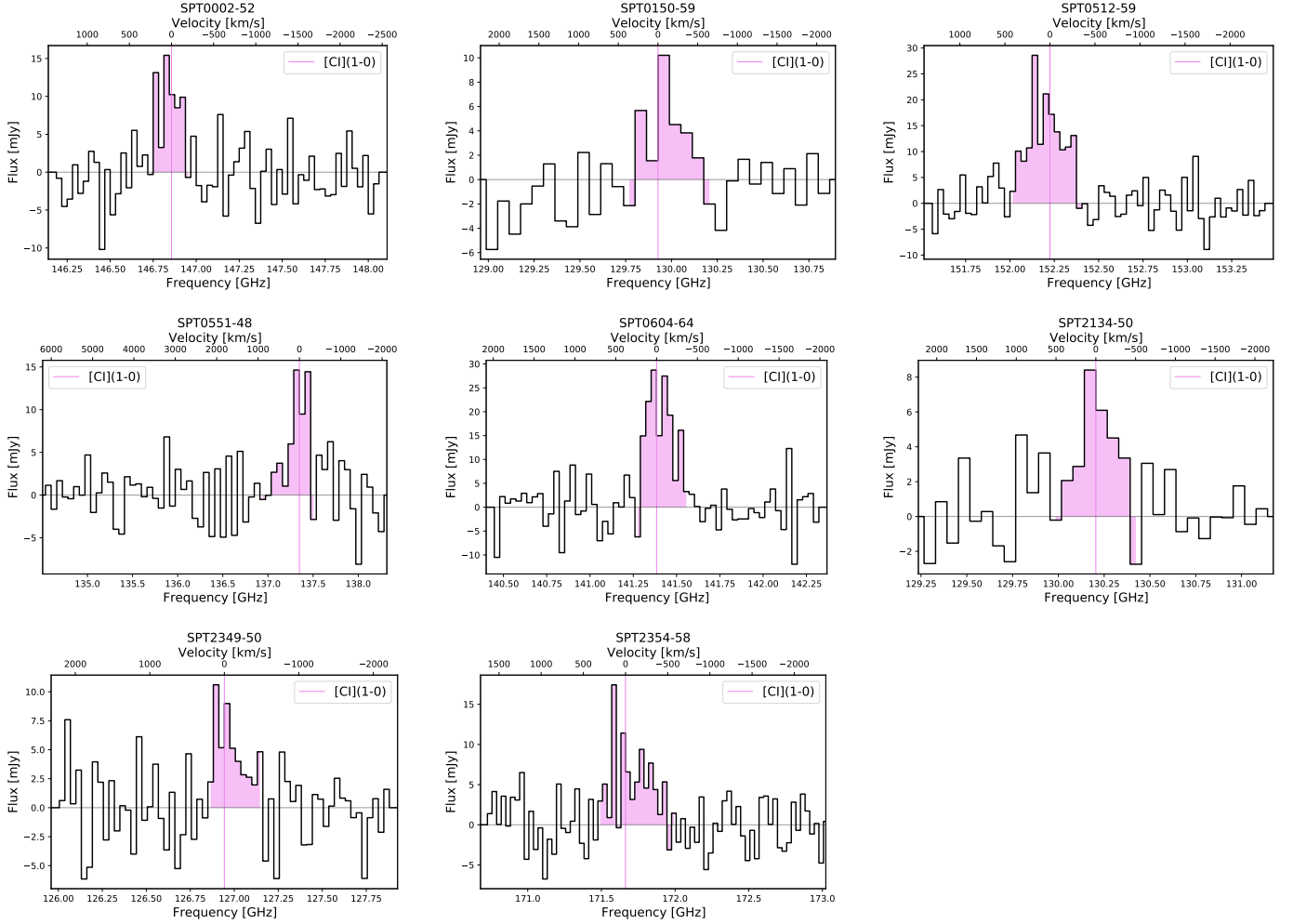


Fig. 1. [CI](1–0) spectra of our sample. The violet dotted line represents the [CI](1–0) line frequency based on the redshifts from Reuter et al. (2020) and the velocity axis is centred at this [CI](1–0) frequency. The violet shaded region represents the integrated limits to compute the integrated intensities of the [CI](1–0) line of our sources.

To estimate the uncertainties on the flux, we selected a polygonal region near the source and measured the noise RMS in this region. The fluxes and their uncertainties for all the lines imaged for our sample are presented in Table 2.

We observed eight sources in [CI](1–0), 6 of which were securely detected ($>5\sigma$) and 2 were tentatively detected ($3 > \sigma > 5$). Of the 29 targets for [CI](2–1), 4 sources were undetected and are presented as 3σ upper-limits, 7 sources were tentatively detected ($3 > \sigma > 5$), and 18 sources were securely detected ($>5\sigma$). The non-detections are presented as 3σ upper limits.

For the ancillary [CI](1–0) data, seven of the sources are tentative detections ($3 < \sigma < 5$) and three are non-detections ($<3\sigma$) from Bothwell et al. (2017) and four sources with tentative detections, one secure detection ($>5\sigma$) and six non-detections from Reuter et al. (2020). From these fluxes we estimated the line luminosities using the formalism from Solomon & Vanden Bout (2005)

$$L_{\text{line}} = 1.04 \times 10^{-3} S_{\nu} \Delta\nu D_L^2 \nu_{\text{obs}} [L_{\odot}], \quad (1)$$

where $S_{\nu} \Delta\nu$ is the integrated intensity (in Jy km s^{-1}) obtained from the moment-0 maps, D_L^2 is the luminosity distance (in Mpc), and ν_{obs} is the observed frequency of the line (in GHz).

4. [CI] line properties

4.1. Relation between [CI] and infrared luminosity

Understanding the relation between the SFR and gas mass for different galaxy populations is crucial in order to decode the nature and evolution of galaxies. The relation between the L_{IR} and $L_{\text{[CI]}}$ can be a proxy to the integrated Kennicutt-Schmidt (KS) law as the bolometric L_{IR} between 8 and $1000 \mu\text{m}$ (L_{IR}) can provide a good estimate of the SFR (Kennicutt 1998; Murphy et al. 2011; Kennicutt & Evans 2012) and the [CI] line can be used to estimate the total molecular gas (e.g., Weiß et al. 2003; Papadopoulos et al. 2004). For our sample we computed the [CI] luminosities using the relation in Eq. (1) with the integrated fluxes estimated from the moment-0 maps (see Sect. 3.2). The L_{IR} for our sample are presented in Reuter et al. (2020) and are based on the *Herschel* and ground-based submillimetre photometry, which provide a very reliable estimate of this quantity. We corrected both the luminosities for their magnification obtained from the lens models presented in Spilker et al. (2016), and assumed a median magnification of 5.5 for sources without reliable lens modelling.

In Fig. 3 we compare the IR luminosity against the luminosities of both [CI] transitions for our sample. The left panel shows the L_{IR} versus the [CI](1–0) luminosity and the right panel presents

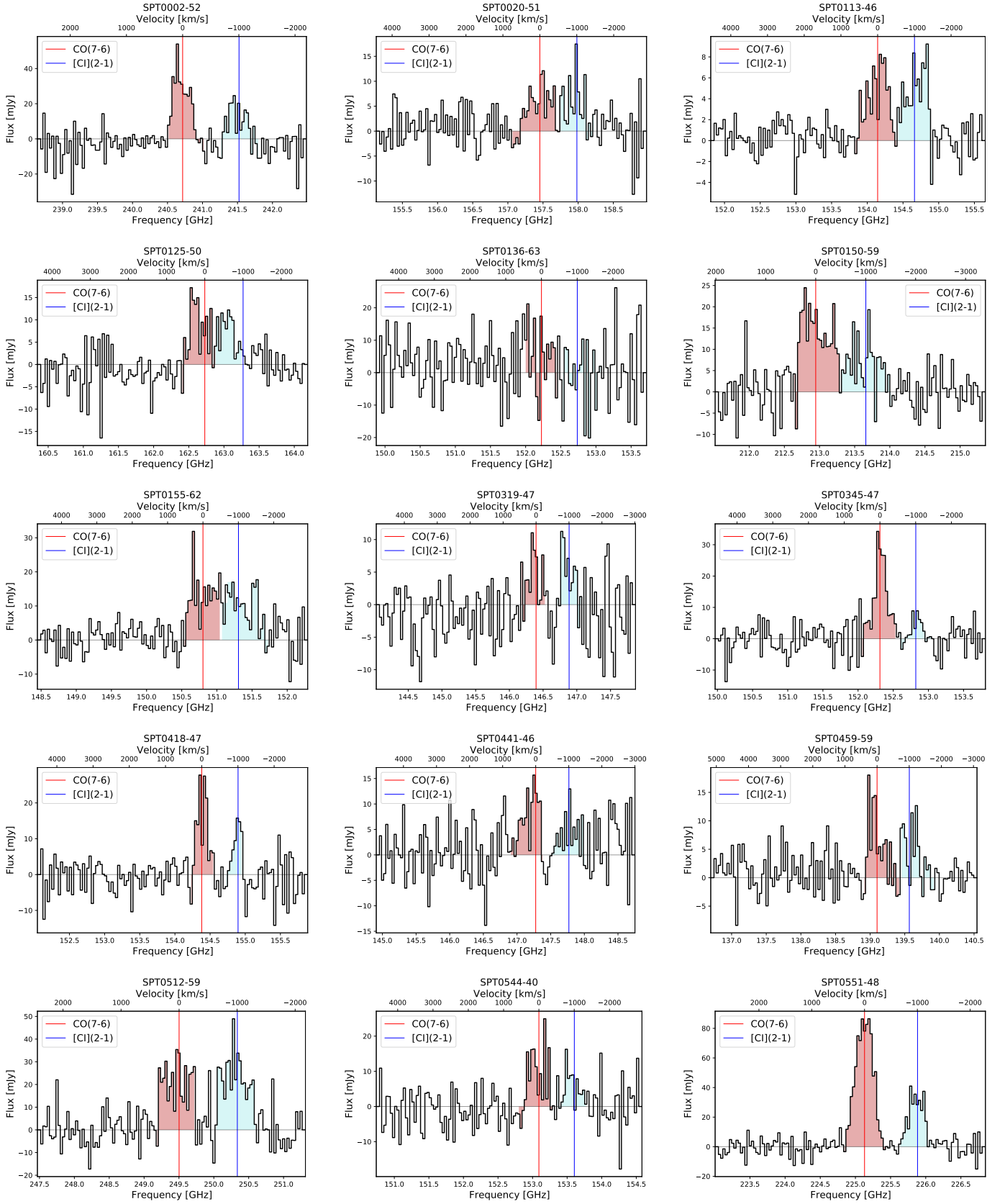


Fig. 2. [CI](2-1) and CO(7-6) spectra of our sample. The red and blue solid lines represent the CO(7-6) and [CI](2-1) frequencies based on the redshifts from Reuter et al. (2020). The velocity axis is centred on this CO(7-6) frequency. The red shaded region is the integration window of the CO(7-6) line and the blue shaded region is the integration window of the [CI](2-1) line. These windows are used to compute the integrated fluxes of the lines.

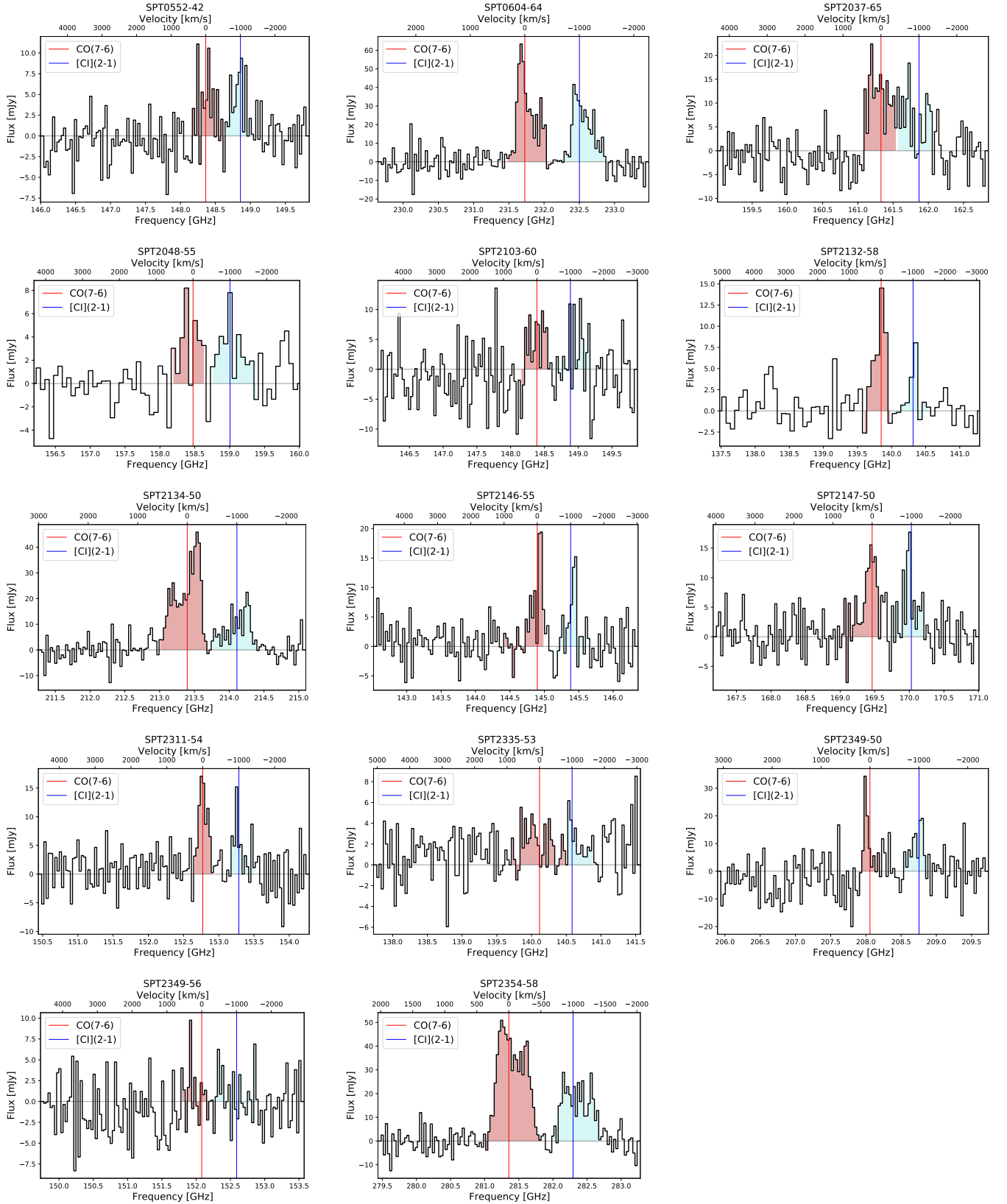


Fig. 2. continued.

the L_{IR} versus the [CII](2–1) luminosity. We fit the relation between the line and the IR luminosity using a linear regression model of Linmix package (Kelly 2007). The slopes and intercept of the fits for both the lines are given in Table 3. Additionally, we compare

our sample with the SMGs, main sequence (MS) at $z \sim 1$, and the local galaxy compilation presented in Valentino et al. (2020) in both the IR-[CII] luminosity plots. We also fit a linear regression model for the SMGs combined with our sample (represented as

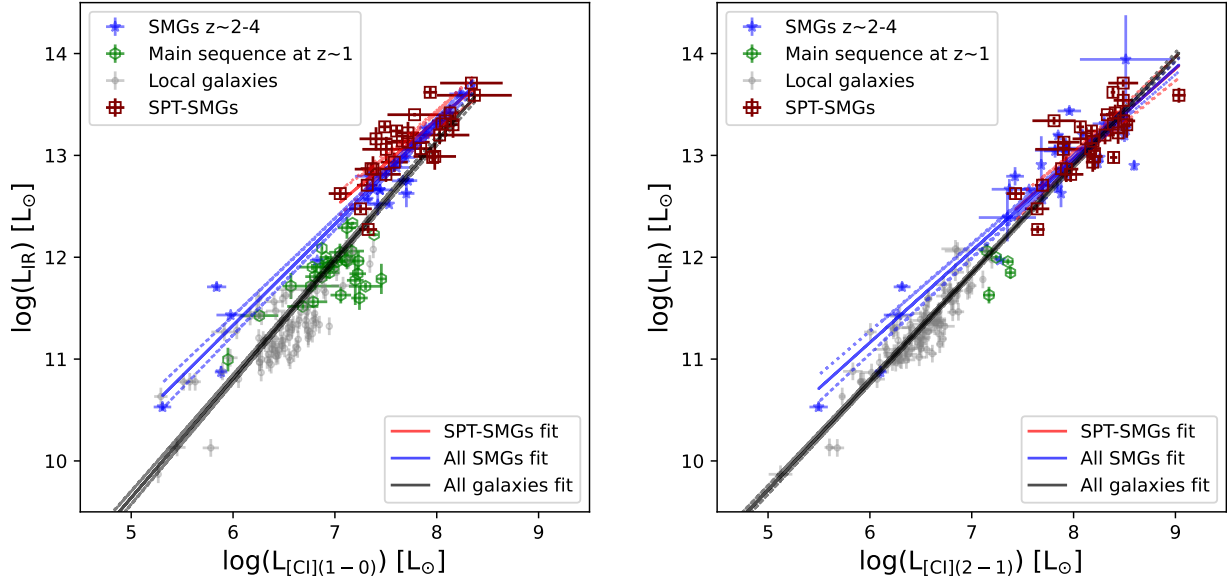


Fig. 3. Infrared luminosities vs. [CI] line luminosities for our sample. The left panel shows the L_{IR} against $L_{\text{[CI]}(1-0)}$ for our sample and the right panel shows the L_{IR} against $L_{\text{[CI]}(2-1)}$ for our sample. Both the luminosities are corrected for magnification and are in units of L_{\odot} . The ACA-[CI] sample is represented by red squares. Our sample is compared with the Valentino et al. (2020) compilation. The blue stars represent the SMGs (Walter et al. 2011; Alaghband-Zadeh et al. 2013; Bothwell et al. 2017; Yang et al. 2017; Andreani et al. 2018; Cañameras et al. 2018; Nesvadba et al. 2019; Dannerbauer et al. 2019; Jin et al. 2019). The main-sequence galaxies at $z \sim 1$ are represented by green hexagons (Valentino et al. 2018; Bourne et al. 2019; Valentino et al. 2020). The local FTS samples of star-forming galaxies are represented by grey circles (Véron-Cetty & Véron 2010; Liu et al. 2015; Kamenetzky et al. 2014). The fit for the entire compilation is represented as the grey solid line. The blue line represents the fit for our sample combined with the literature SMGs, and the red line represents the fit for our sample. The 1σ limit of the fit is represented as dashed lines.

Table 3. Fit parameters of the L_{IR} vs. $L_{\text{[CI]}}$ for all the samples in Fig. 1.

Sample	Slope (β) [CI](1-0) dex	Intercept (α) [CI](1-0) dex	Slope (β) [CI](2-1) dex	Intercept (α) [CI](2-1) dex
SPT-SMGs	0.90 ± 0.17	6.14 ± 1.28	0.88 ± 0.14	5.94 ± 1.11
All SMGs	1.00 ± 0.05	5.34 ± 0.41	0.90 ± 0.05	5.77 ± 0.42
Local galaxies and main-sequence at $z \sim 1$	0.98 ± 0.04	4.95 ± 0.23	1.02 ± 0.03	4.63 ± 0.19
Full sample	1.16 ± 0.03	3.83 ± 0.21	1.06 ± 0.02	4.40 ± 0.13

Notes. All the fit parameters are from the Linmix linear-regression fitting module. The errors on the slopes and intercepts are from the MCMC chain posteriors in the Linmix linear-regression fitting module.

all SMGs in Fig. 3), for the local galaxies and the main-sequence galaxies, and for the entire galaxy population including our sample. For both the [CI]-lines, the IR versus [CI] luminosity relation exhibits a slight variation in slopes between the different populations shown in Fig. 3 and Table 3. In the case of the L_{IR} versus $L_{\text{[CI]}(1-0)}$ relation, our sample (SPT-SMGs, 0.90 ± 0.17) and our compilation of SMGs (1.00 ± 0.05) are both compatible at 1σ with a linear relation. However, our sample of SPT-SMGs span across a small range of luminosities, thereby making their slopes uncertain. The local and $z \sim 1$ main-sequence galaxies also have a similar slope (0.98 ± 0.04) to the SPT-SMGs and the combined SMG sample, but the slope of the combined samples containing all the galaxies is higher (1.16 ± 0.03). In the case of L_{IR} versus $L_{\text{[CI]}(2-1)}$ relation, the slopes are a little flatter for SPT-SMGs (0.88 ± 0.14) and all SMGs (0.9 ± 0.05) compared to the linear slopes for the local galaxies (1.02 ± 0.03) and the combined population (1.06 ± 0.02). The slopes remain nearly linear across all populations.

We compare our observed slopes with the L_{FIR} or L_{IR} to $L'_{\text{CO}(1-0)}$ best-fit relation presented in Greve et al. (2014), Liu et al.

(2015), and Kamenetzky et al. (2016). Since CO ($n_{\text{crit}}\text{CO}(1-0) \sim 2.1 \times 10^3 \text{ cm}^{-3}$ and $n_{\text{crit}}\text{CO}(2-1) \sim 1.1 \times 10^4 \text{ cm}^{-3}$) and [CI] ($n_{\text{crit}}[\text{CI}](1-0) \sim 4.7 \times 10^2 \text{ cm}^{-3}$ and $n_{\text{crit}}[\text{CI}](2-1) \sim 1.2 \times 10^3 \text{ cm}^{-3}$) are both tracers of the cold gas, we could expect to find similar results. However, this is not trivial because [CI] traces lower density gas than CO. In the case of Greve et al. (2014), they find a slope of 1.00 ± 0.05 for L_{IR} versus $L'_{\text{CO}(1-0)}$ and 1.05 ± 0.10 for L_{IR} versus $L'_{\text{CO}(2-1)}$ relation for a sample of local ULIRGs and $z > 1$ DSFGs, which agrees with our slope of L_{IR} versus $L_{\text{[CI]}(1-0)}$ for the combined SMG sample and the sample of local galaxies and $z \sim 1$ main-sequence galaxies. Kamenetzky et al. (2016) found a slope of 1.27 ± 0.04 for the L_{FIR} versus $L'_{\text{CO}(1-0)}$ relation in a sample of galaxies: active galactic nuclei (AGNs), main-sequence galaxies, and ULIRGs. In the case of their subsample of ULIRGs, they found a lower slope of 1.15 ± 0.09 than for the full sample as we found for [CI](1-0), but their slope is in 1.5σ tension with unity.

The slope variations in relations between gas mass tracers ([CI](1-0) or low- J CO) and SFR tracers (L_{IR}) for different

populations such as starbursts and main-sequence galaxies, has been previously explored (e.g., [Daddi et al. 2010b](#); [Genzel et al. 2010](#)). [Daddi et al. \(2010b\)](#) suggest that this could be due to the two populations having a different SFR–gas mass relation. Starbursts are expected to have less gas for the same SFR, and to thus have a lower [CI] or CO luminosity. Since the low- L_{IR} galaxies are mainly on the main sequence and the bright galaxies are more often starbursts (e.g., [Sargent et al. 2012](#)), this could lead to a steeper slope for the full sample containing both populations.

In the case of the L_{IR} versus $L_{\text{[CI](2-1)}}$ relation, slopes of 0.90 ± 0.05 for the combined SMGs and 0.88 ± 0.14 for the SPT-SMGs are comparable to the mid- J CO versus L_{FIR} slopes (0.94 ± 0.11 for CO(3–2) for the ULIRG sample) found in [Kamenetzky et al. \(2016\)](#). We also find that the local and main-sequence galaxies have nearly the same [CI](1–0)/IR luminosity ratios, but lower [CI](2–1)/IR ratios compared to the SMGs and SPT-SMG sample. The difference in trends for starbursts and main-sequence galaxies, as seen in the case of [CI](1–0), may not be significant for [CI](2–1) due to the excitation of the CO and [CI] being higher for starbursts. For the higher energy transition this compensates for the lower gas content; the main-sequence and starburst galaxies have similar relations. We cannot constrain the stellar-mass to SFR relation (position relative to the main sequence) for these galaxies due to the unavailability of stellar mass estimates based on the photometry. From the stellar mass estimates of [Ma et al. \(2015\)](#), SPT-SMGs in their analysis were found to be possibly representative of a starburst population. However, due to the sample size and the uncertainties in the stellar-mass estimates, it is difficult to determine whether these galaxies represent a starbursting population or an extended main-sequence population.

4.2. [CI] excitation temperature

The excitation temperature of [CI] can be estimated from the line luminosity ratio of the two [CI] transitions, $R_{\text{CI}} = L'_{\text{[CI](2-1)}}/L'_{\text{[CI](1-0)}}$ for an optically thin scenario ([Stutzki et al. 1997](#); [Weiß et al. 2003](#); [Walter et al. 2011](#)). The excitation temperature, T_{ex} is computed as

$$T_{\text{ex}} = \frac{38.8}{\ln\left(\frac{2.11}{R_{\text{CI}}}\right)} \text{ [K]}.$$

For the sources at least tentatively detected in both the [CI] transitions, we can directly derive the excitation temperature and its uncertainties. To estimate the uncertainties of the excitation temperature, we make a simulation with the observed [CI] fluxes. We generate a random Gaussian distribution with each of the [CI] fluxes with the width of the distribution derived from the error of the fluxes. For each of these points, we compute the excitation temperature and generate asymmetrical error bars on this distribution as the 16th and 84th percentile. Galaxies with only one [CI] transition tentatively detected are considered as upper limits or lower limits.

The excitation temperature of our sample varies from 17.7 to 64.2 K with a mean value of 34.5 ± 2.1 K. These temperatures are slightly higher than the mean temperatures reported in [Valentino et al. \(2020\)](#) ($\langle T_{\text{ex}} \rangle = 25.6 \pm 1.0$ K) and [Nesvadba et al. \(2019\)](#) ($T_{\text{ex}} = 21\text{--}37$ K), but are comparable to the mean temperature reported in [Walter et al. \(2011\)](#) ($\langle T_{\text{ex}} \rangle = 29.1 \pm 6.3$ K). Overall, our temperatures are slightly higher than the commonly adopted [CI] excitation temperature of $T_{\text{ex}} = 30$ K ([Alaghband-Zadeh et al. 2013](#); [Bothwell et al. 2017](#)), but compatible to a 2σ level.

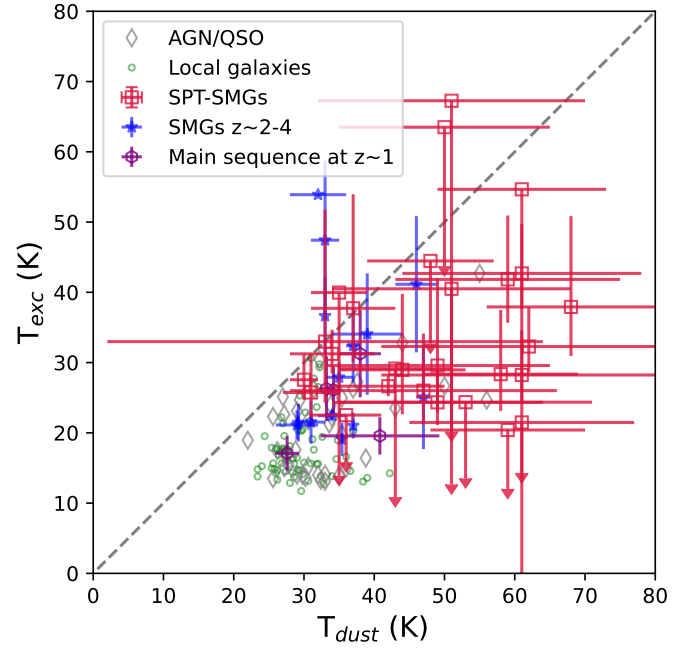


Fig. 4. [CI] excitation vs. dust temperature for our sample. Our sources are represented as red-squares. Sources with 1σ to 3σ detections in either or both [CI] lines are represented as upper-limits. The dust temperatures for our sample are from the SED fits of [Reuter et al. \(2020\)](#). Also compared are the excitation temperatures of SMGs (blue stars), main-sequence galaxies at $z \sim 1$ (purple hexagons), local galaxies (green points), and AGNs (grey diamonds) from the [Valentino et al. \(2020\)](#) compilation. The grey dashed line corresponds to the 1:1 relation between the dust and [CI] excitation temperatures.

[Reuter et al. \(2020\)](#) presents the dust mass and dust temperatures for the SPT-SMGs by fitting the SED using a modified black-body law. They fix the Rayleigh-Jeans spectral slope, β to 2, to mitigate degeneracies between redshift and dust temperature and reduce the number of free parameters. Additionally, they also define λ_0 as a function of T_{dust} using the empirical relation provided by [Spilker et al. \(2016\)](#). Thus, only three free parameters, photometric redshift, dust temperature (T_{dust}), and the overall SED normalisation, are used in the SED fitting procedure.²

In Fig. 4 we compare the [CI] excitation temperature to the dust temperatures for our sample. In general, for all our sources (with secure estimates of T_{ex}), $T_{\text{ex}} \lesssim T_{\text{dust}}$. These results agree with the SMG population from [Nesvadba et al. \(2019\)](#) and with the compilation of galaxies presented in [Valentino et al. \(2020\)](#). Furthermore, we find results similar to those of [Bothwell et al. \(2017\)](#): $T_{\text{kin}} < T_{\text{dust}}$ for SPT-SMGs, assuming $T_{\text{kin}} = T_{\text{ex}}$ at LTE. In Fig. 4 we also plot the SMGs, main-sequence galaxies, and local galaxies from the compilation sample presented in [Valentino et al. \(2020\)](#). Overall, our sources seem to have a higher dust and excitation temperature compared to the local galaxies and main-sequence galaxies, but comparable excitation temperatures to the SMGs.

The dust temperature could be used as a proxy to the excitation or gas temperature due to the gas to dust coupling, assuming an LTE condition (e.g., [Narayanan et al. 2011](#); [Carilli & Walter 2013](#); [da Cunha et al. 2013](#)). From our results and the previous

² We refer to [Reuter et al. \(2020\)](#) for details on the SED fitting and the estimation of dust temperatures and dust masses that are used in this work.

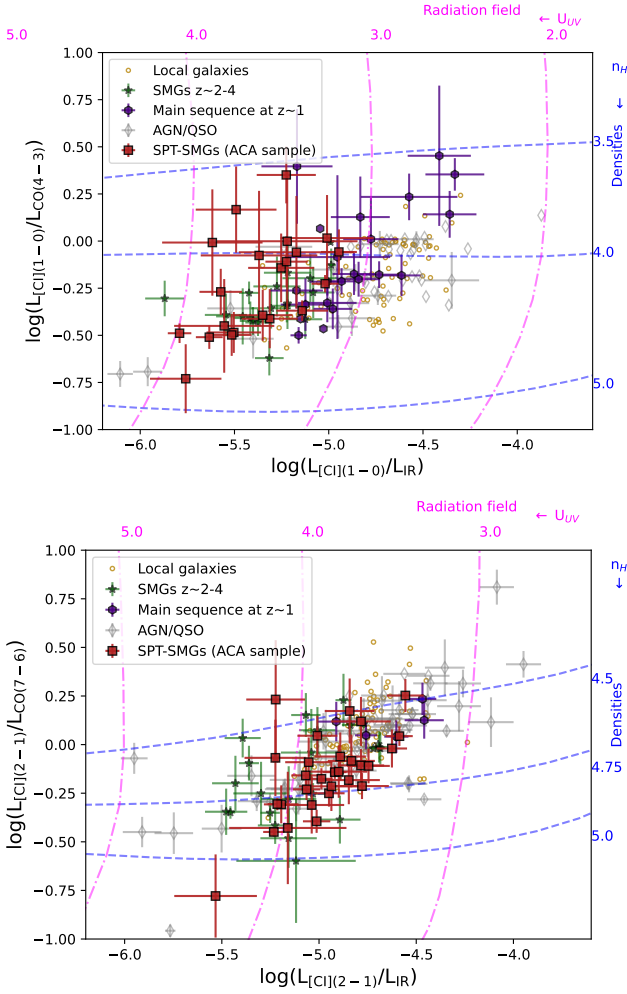


Fig. 5. $L_{\text{CII}(1-0)}/L_{\text{CO}(4-3)}$ vs. $L_{\text{CII}(1-0)}/L_{\text{IR}}$ in the top panel and $L_{\text{CII}(2-1)}/L_{\text{CO}(7-6)}$ vs. $L_{\text{CII}(2-1)}/L_{\text{IR}}$ in the bottom panel for our sample. Our sources are represented as red squares. The SMGs (dark green stars), main-sequence galaxies at $z \sim 1$ (indigo hexagons), local galaxies (gold empty circles), and AGNs (grey diamonds) from the Valentino et al. (2020) compilation are plotted along with our sample. The isocontours of density and radiation field intensity are plotted as grey dashed and grey dot-dashed lines, respectively. These isocontours are obtained from the PDR modelling of Kaufman et al. (2006) from the PDR toolbox (Pound & Wolfire 2023). The individual luminosities are not corrected for magnification.

studies mentioned above, we find a lower gas excitation than the dust temperature systematically. This could be explained by the gas and dust not being in thermal equilibrium (Cañameras et al. 2015; Nesvadba et al. 2019). Furthermore, the dust and [CII] emission may not be originating from the same phase of the ISM. The dust emission can be dominated by the central star-forming regions, whereas [CII] could trace cooler extended regions (e.g., Valentino et al. 2018; Nesvadba et al. 2019). The SPT-SMGs have a higher dust temperature compared to the other populations in Fig. 4. However, comparing the dust temperatures between different samples is potentially biased due to the differences in the parametrisation of the SED modelling and/or the different sampling of the dust SED.

Cortzen et al. (2020) compared the [CII] excitation temperatures of GN20, a starburst at $z \sim 4$ to its dust temperature. They found a [CII] excitation temperature of $T_{\text{ex}} = 48.2^{+15.1}_{-9.2}$ K for the galaxy, compared to the dust temperature, $T_{\text{dust}} = 33 \pm 2$ K using

an SED modelling with an optically thin regime. This strong outlier suggested that the dust could be optically thick, thereby appearing deceptively cold. Hence, with the optically thick dust, they estimated $T_{\text{dust}} = 52 \pm 5$ K, which was more agreeable with the excitation temperature. In our sample we do not find candidates hinting at optically thick dust component, thus suggesting that GN20 could be an exception.

However, the recent works of Papadopoulos et al. (2022) concluded that [CII] line excitation is subthermal and excitation temperatures cannot be derived with the line ratios assuming an LTE condition. Furthermore, they concluded that non-LTE [CII] line ratios could be used to constrain the dust SED models rather than estimating the [CII] excitation.

4.3. ISM diagnostics with line ratios

Line ratios can be used as a tracer of ISM properties of galaxies. A ratio of an extended gas tracer such as [CII] (Papadopoulos et al. 2004; Papadopoulos & Greve 2004; Walter et al. 2011; Bothwell et al. 2017) and a relatively dense gas tracer such as high- J CO can be a proxy to the density of the ISM. We computed the $L_{\text{CII}(1-0)}/L_{\text{CO}(4-3)}$ and $L_{\text{CII}(2-1)}/L_{\text{CO}(7-6)}$ ratios for our sample. The choice of the CO transitions is due to the close spectral proximity of the lines to the [CII] spectral frequencies at these redshifts. The CO(7-6) and [CII](2-1) lines can be imaged in the same spectral window at these redshifts. Similarly, the [CII](1-0) and CO(4-3) can also be observed in a single frequency range for some of these galaxies. We compared these [CII]-to-CO luminosity ratios with the [CII]-IR luminosity ratio. [CII] being an extended gas tracer can be a proxy to the gas mass and IR luminosity traces the star formation, thus this ratio is a tracer of the radiation field of the ISM.

Figure 5 shows the $L_{\text{CII}(1-0)}/L_{\text{CO}(4-3)}$ versus $L_{\text{CII}(1-0)}/L_{\text{IR}}$ in the top panel and $L_{\text{CII}(2-1)}/L_{\text{CO}(7-6)}$ versus $L_{\text{CII}(2-1)}/L_{\text{IR}}$ in the bottom panel. We also compare the isocontours of the density and radiation field from the PDR modelling of Kaufman et al. (2006) available from the PDR-toolbox (Pound & Wolfire 2023) with our sample in Fig. 5. However, there are some caveats in comparing line ratios to PDR models. The line emission may not arise from the same region of the PDRs, and they cannot fully reproduce the line excitation in starbursts without additional heating mechanisms (e.g., Papadopoulos et al. 2012). Additionally, a part of the IR emission can arise from the HII regions, and hence may not be reproduced by PDRs. The IR emission arising from the warm dust may also be responsible for the heating mechanisms of the sources (Valentino et al. 2018).

We compare our sample with the compilation presented in Valentino et al. (2020), consisting of SMGs, main-sequence galaxies at $z \sim 1$, and local galaxies. In the $L_{\text{CII}(1-0)}/L_{\text{CO}(4-3)}$ versus $L_{\text{CII}(1-0)}/L_{\text{IR}}$ plot (top panel, Fig. 5), our sample has a lower $L_{\text{CII}(1-0)}/L_{\text{IR}}$ ratio compared to the local galaxies and the main-sequence galaxies at $z \sim 1$ with an overlap. In terms of the $L_{\text{CII}(1-0)}/L_{\text{CO}(4-3)}$ ratios, they have similar values as main-sequence galaxies and the SMGs.

While comparing the $L_{\text{CII}(2-1)}/L_{\text{CO}(7-6)}$ versus $L_{\text{CII}(2-1)}/L_{\text{IR}}$ (bottom panel, Fig. 5), our sample has comparable $L_{\text{CII}(2-1)}/L_{\text{IR}}$ with the SMGs, main-sequence galaxies, and local galaxies. In terms of the $L_{\text{CII}(2-1)}/L_{\text{CO}(7-6)}$ ratio, they are at the lower end in comparison to the main-sequence and local galaxies. The difference in trends between populations for the [CII]/CO ratio could arise due to the variation in CO-SLEDs at high- J CO lines for the different populations, but not in the mid- J CO lines (e.g., Casey et al. 2014; Liu et al. 2015; Daddi et al. 2015; Yang et al. 2017; Cañameras et al. 2018;

Valentino et al. 2020). Furthermore, the galaxies with higher densities also have a stronger radiation field intensity.

To summarise, the differences in line ratios between the populations when compared to the PDR models suggest that our sample and the SMGs have comparable densities to the main-sequence and local galaxies, but lower radiation field intensities despite an overlap. In both these plots, our sources are diverse, with radiation field intensities ranging from $10^{2.5}$ to $10^{4.5}$ Habing units and densities ranging from 3.5 to 5.0 cm^{-3} . However, all the ratios in Fig. 5 are not corrected for magnification assuming the contribution of differential magnification might not be very significant ($<24\%$ found in the analysis of SPT-SMGs from Gururajan et al. 2022).

5. Comparison of [CI] with other gas tracers

5.1. Estimation of the gas mass

We compare the ability of [CI] as an estimator of molecular gas mass of the galaxies against traditionally used gas-mass tracers such CO(1–0) emission line, the dust mass, and the [CII] line emission. We estimate the molecular gas mass using the four tracers to test their agreement or disagreement with each other.

5.1.1. [CI]-based gas masses

One of the methods of estimating of [CI]-based molecular gas mass was introduced by Papadopoulos & Greve (2004) as

$$M(\text{H}_2)^{[\text{CI}]} = 1375.8 \times 10^{-12} \frac{D_L^2 S_\nu \Delta\nu}{(1+z) A_{10} Q_{10} X_{\text{CI}}} [M_\odot], \quad (2)$$

where D_L is the luminosity distance to the galaxy in Mpc, $A_{10} = 0.793 \times 10^{-7} \text{ s}^{-1}$ is the Einstein coefficient, $S_\nu \Delta\nu$ is the integrated intensity in Jy km s^{-1} , and z is the redshift. The above equation can be rewritten in terms of [CI] luminosity, $L_{[\text{CI}]} [L_\odot]$ with $A_{10} = 0.793 \times 10^{-7} \text{ s}^{-1}$, and $\nu_{\text{rest},[\text{CI}]} = 492.16 \text{ GHz}$ as

$$M(\text{H}_2)^{[\text{CI}]} = 3.39 \times 10^{-2} \frac{L_{[\text{CI}]}}{Q_{10} X_{\text{CI}}} [M_\odot]. \quad (3)$$

The main uncertainties in the gas mass estimated from [CI] arise from assumptions of the [CI]-excitation factor/partition function, Q_{10} , and the [CI]/ H_2 abundance ratio, X_{CI} .

The [CI] excitation factor depends on the excitation conditions in the gas such as the temperature and the critical densities. The excitation factor of level $J = 1$ to $J = 0$ can be derived as³

$$Q_{10} = \frac{3e^{-T_1/T_{\text{ex}}}}{1 + 3e^{-T_1/T_{\text{ex}}} + 5e^{-T_2/T_{\text{ex}}}}, \quad (4)$$

where $T_1 = 23.6 \text{ K}$ and $T_2 = 62.5 \text{ K}$ are the excitation energy levels of atomic carbon and T_{ex} is the excitation temperature of the ISM. Since we estimated the excitation temperature for most of our sources, we can constrain the gas mass without assuming a value for the [CI] excitation factor. Our sample has a median Q_{10} value of 0.45 ± 0.01 , which is in agreement with the median value of 0.43 for the sample presented in Dunne et al. (2021), and the values used in Papadopoulos et al. (2004), Alaghband-Zadeh et al. (2013) and Nesvadba et al. (2019). These values are lower than the Q_{10} value of 0.6 assumed in Bothwell et al. (2017), thereby giving us a higher mass estimate. Thus, in our sample the only unknown for the [CI]-based gas mass estimates would be the [CI]/ H_2 abundance ratio, X_{CI} .

³ We refer to Appendix A of Papadopoulos et al. (2004) for an extended in-depth derivation of the excitation factor, in particular Eqs. (A8) and (A15).

5.1.2. CO-based gas masses

The total molecular gas mass from CO(1–0) line observations can be estimated using the following relation:

$$M(\text{H}_2)^{\text{CO}} = \alpha_{\text{CO}} L'_{\text{CO}(1-0)} [M_\odot]. \quad (5)$$

Here $L'_{\text{CO}(1-0)}$ is the line luminosity of CO(1–0) in $\text{K km s}^{-1} \text{ pc}^2$ and α_{CO} is the CO-to- H_2 conversion factor with the units, $M_\odot [\text{K km s}^{-1} \text{ pc}^2]^{-1}$.

The main uncertainty for the CO-based molecular gas mass estimates arises from the α_{CO} factor. In addition, since the CO(1–0) transition cannot be observed for most of these galaxies, we use CO-SLEDs to derive the CO(1–0) fluxes from the other observed low- J and mid- J transitions. Three of our sources have CO(1–0) and 8 of our sources have CO(2–1) line fluxes from the ATCA observations presented in Aravena et al. (2016). We also have CO(3–2) and CO(4–3) fluxes from the ALMA band-3 spectral scans (Reuter et al. 2020). To compute the gas mass, we use the lowest- J transition available for our sources, up to the CO(4–3) transition. The line luminosity ratios to obtain the CO(1–0) luminosities are from Spilker et al. (2014) and Harrington et al. (2021) for the SMGs. We use $R_{21} = 0.88 \pm 0.07$, $R_{32} = 0.69 \pm 0.12$, and $R_{43} = 0.52 \pm 0.14$.

The α_{CO} factor is debated in the literature, and can vary from 0.8 for ULIRGs or starburst-like environments (e.g., Downes & Solomon 1998) to higher value of ~ 4.4 for Milky Way-like galaxies (e.g., Solomon et al. 1987; Strong & Mattox 1996; Abdo et al. 2010) and have also been independently estimated for SMGs (e.g., Spilker et al. 2015; Calistro Rivera et al. 2018). The choice of α_{CO} could thus give a gas mass varying by nearly a factor of 5 . This factor, therefore, contributes to the main uncertainty for the gas mass estimated from CO luminosity.

5.1.3. Dust-based gas masses

The gas mass can be estimated from the dust mass assuming a gas-to-dust ratio

$$M(\text{H}_2)^{\text{dust}} = \delta_{\text{GDR}} M_{\text{dust}} [M_\odot], \quad (6)$$

where M_{dust} is the dust mass of the galaxy in M_\odot units and δ_{GDR} is the assumed gas-to-dust ratio. To have a good estimate of the dust mass, we need to model the SED of the galaxy, which in turn depends on certain factors. Constraining the peak of the SED from space-based observations (e.g., Herschel) along with a good sampling of the Rayleigh-Jeans tail from millimetric ground-based observations can help improve the SED fitting. Additionally, constraining the dust emissivity index as a function of the dust continuum can reduce the number of free parameters in the SED fitting and provide a better constraint on the dust mass. The gas-to-dust ratio is known to vary with metallicity (e.g., Magdis et al. 2011; Leroy et al. 2011; Popping & Péroux 2022; Popping et al. 2023). The assumed gas-to-dust ratio is therefore the main factor contributing to the uncertainties in the dust mass derived gas mass.

5.1.4. [CII]-based gas masses

Zanella et al. (2018) proposed the following calibration relation to estimate the [CII]-based molecular gas mass:

$$M(\text{H}_2)^{[\text{CII}]} = \alpha_{[\text{CII}]} L_{[\text{CII}]} [M_\odot]. \quad (7)$$

Here $\alpha_{[\text{CII}]}$ is the [CII]-to- H_2 conversion factor with the units $M_\odot L_\odot^{-1}$ and $L_{[\text{CII}]}$ is the line luminosity in L_\odot . They reported

a median value of $\alpha_{[\text{CII}]} \sim 31 M_{\odot}/L_{\odot}$ and a median absolute deviation of 0.2 dex. Zanella et al. (2018) also found that $\alpha_{[\text{CII}]}$ remains unaffected by metallicity or star formation modes. This is in contrast to the other three tracers we consider where the main limitations arise from the conversion factors, such as α_{CO} , X_{Cl} , and δ_{GDR} .

5.2. Cross-calibration of the various gas conversion factors

From our four gas mass tracers we have four unknown factors. Since the absolute values of all these tracers depend on various factors and are highly debated, we cross-calibrate these tracers to test the agreement between them. Assuming that the gas mass estimated from each of these tracers are equivalent, we can obtain the following relations:

for α_{CO} and X_{Cl} , from equation Eqs. (3) and (5):

$$\begin{aligned} M(\text{H}_2)^{\text{CO}} &= M(\text{H}_2)^{[\text{Cl}]} \\ \Rightarrow \frac{3.39 \times 10^{-2} L_{[\text{Cl}]}}{Q_{10} L'_{\text{CO}(1-0)}} &= X_{\text{Cl}} \times \alpha_{\text{CO}}; \end{aligned} \quad (8)$$

for δ_{GDR} and X_{Cl} , from equation Eqs. (3) and (6):

$$\begin{aligned} M(\text{H}_2)^{\text{dust}} &= M(\text{H}_2)^{[\text{Cl}]} \\ \Rightarrow \frac{3.39 \times 10^{-2} L_{[\text{Cl}]}}{Q_{10} M_{\text{dust}}} &= X_{\text{Cl}} \times \delta_{\text{GDR}}; \end{aligned} \quad (9)$$

and for δ_{GDR} and α_{CO} , from equation Eqs. (6) and (5):

$$\begin{aligned} M(\text{H}_2)^{\text{dust}} &= M(\text{H}_2)^{\text{CO}} \\ \Rightarrow \frac{L'_{\text{CO}(1-0)}}{M_{\text{dust}}} &= \frac{\delta_{\text{GDR}}}{\alpha_{\text{CO}}}; \end{aligned} \quad (10)$$

for $\alpha_{[\text{CII}]}$ and X_{Cl} , from equation Eqs. (3) and (7):

$$\begin{aligned} M(\text{H}_2)^{[\text{CII}]} &= M(\text{H}_2)^{[\text{Cl}]} \\ \Rightarrow \frac{3.39 \times 10^{-2} L_{[\text{Cl}]}}{Q_{10} L_{[\text{CII}]}} &= X_{\text{Cl}} \times \alpha_{[\text{CII}]}; \end{aligned} \quad (11)$$

for δ_{GDR} and $\alpha_{[\text{CII}]}$, from equation Eqs. (7) and (6):

$$\begin{aligned} M(\text{H}_2)^{\text{dust}} &= M(\text{H}_2)^{[\text{CII}]} \\ \Rightarrow \frac{L_{[\text{CII}]}}{M_{\text{dust}}} &= \frac{\delta_{\text{GDR}}}{\alpha_{[\text{CII}]}}, \end{aligned} \quad (12)$$

and for $\alpha_{[\text{CII}]}$ and α_{CO} , from equation Eqs. (7) and (5):

$$\begin{aligned} M(\text{H}_2)^{[\text{CII}]} &= M(\text{H}_2)^{\text{CO}} \\ \Rightarrow \frac{L_{[\text{CII}]}}{L'_{\text{CO}(1-0)}} &= \frac{\alpha_{\text{CO}}}{\alpha_{[\text{CII}]}}, \end{aligned} \quad (13)$$

These equations only provide a ratio or product of the unknowns, α_{CO} , X_{Cl} , δ_{GDR} , and $\alpha_{[\text{CII}]}$ in terms of all the other observables. In this way we do not have to assume an absolute value for any quantity since all four unknowns have their limitations. We can obtain a mean value for the cross-calibration of our sample and test its agreement with different values found in the literature.

In Fig. 6 we plot the six ratios as a function of L_{IR} . We do not correct the fluxes or dust mass for magnification as we compute the ratio, although there might be small biases due to differential magnification. For the plots comparing the α_{CO} , we indicate the CO transition used to compute the $L'_{\text{CO}(1-0)}$ to further check if there is an agreement between the different transitions.

In the left column of Fig. 6 we compare the $X_{\text{Cl}} \times \alpha_{\text{CO}}$, $X_{\text{Cl}} \times \alpha_{[\text{CII}]}$, and $X_{\text{Cl}} \times \delta_{\text{GDR}}$ against the L_{IR} . In the right column of Fig. 6 we compare $\alpha_{\text{CO}}/\alpha_{[\text{CII}]}$, $\delta_{\text{GDR}}/\alpha_{\text{CO}}$, and $\delta_{\text{GDR}}/\alpha_{[\text{CII}]}$ against the L_{IR} . We also include the sample of nearby ($z \sim 0.3$) galaxies presented in Dunne et al. (2021) and the compilation of SMGs, main-sequence galaxies, and local galaxies presented in Valentino et al. (2020) when the data are available.

We compute the internal scatter of the sample and probe any underlying trends with Linmix (Kelly 2007). It is a Bayesian linear regression fitting model that can fit data with errors along with the upper limits. The intercept, the slope, and the internal scatter of the sample from the fit are summarised in Table A.1.

Comparing the dependence of these tracers on L_{IR} , the slope is compatible with 0, and thus we can compute directly a constant conversion factor. We can also see that the scatter is small; the maximum scatter is 0.4 dex for $\delta_{\text{GDR}}/\alpha_{[\text{CII}]}$. The four estimators are thus remarkably consistent for this population. In the case of $X_{\text{Cl}} \times \alpha_{\text{CO}}$ versus L_{IR} and $\alpha_{\text{CO}}/\alpha_{[\text{CII}]}$ versus L_{IR} there is a good agreement with our estimates using the different CO lines.

On comparing the $X_{\text{Cl}} \times \alpha_{\text{CO}}$ relation for our sources with the literature, we find a ratio similar to that in the sample presented in Dunne et al. (2021). Some of the sources from the Valentino et al. (2020) have a higher value of $X_{\text{Cl}} \times \alpha_{\text{CO}}$, and most of these extreme sources are dominated by AGNs. In the case of $\delta_{\text{GDR}}/\alpha_{\text{CO}}$ and $X_{\text{Cl}} \times \delta_{\text{GDR}}$ versus L_{IR} we see a tight correlation of these tracers and a good agreement with the Dunne et al. (2021) sample. In general, we do not see any trend of these tracers with L_{IR} for our sample, and all the tracers are in reasonably tight correlation with less than 0.41 dex scatter.

In Fig. A.1 we compare these tracers against the dust temperature. For $X_{\text{Cl}} \times \alpha_{\text{CO}}$ versus T_{dust} we do not see a trend with temperature, and for $X_{\text{Cl}} \times \delta_{\text{GDR}}$, $\alpha_{\text{CO}}/\alpha_{[\text{CII}]}$, and $\delta_{\text{GDR}}/\alpha_{[\text{CII}]}$ we do not see a significant trend ($< 1\sigma$). On the other hand, we see a possible trend ($\sim 2.5\sigma$) for $\delta_{\text{GDR}}/\alpha_{\text{CO}}$ with T_{dust} . This could originate from the degeneracy between the dust temperature and the dust mass in the SED modelling. One way to break this is by better sampling the SED and improving the modelling.

6. Discussion

6.1. Origin of the scatter between the various tracers

We found a small scatter for all the cross-calibration relations in Fig. 6. To understand the origin of this scatter, we performed a simulation to test the contribution of measurement uncertainty on this scatter. This procedure is described in Appendix D. Figure D.1 shows the comparison of the mock data with measurement error (in red) with the observed data (in black) for all our sources. For our cross-calibration relations, a significant fraction of this scatter can be reproduced by measurement uncertainties, and the Kolmogorov-Smirnov (KS) test shows that the distribution of the measurements and of a simulation, assuming a perfectly tight relation and only measurement uncertainties, are similar. However, even if we cannot detect it, there is certainly an intrinsic scatter between the tracers.

6.2. Understanding the cross-calibration of tracers

Overall, the various tracers agree with each other within a $\lesssim 0.4$ dex scatter, and we do not see any trend in comparing them with the L_{IR} . The mean values of the cross-calibration are given in Table 4. Here we discuss the impact of the assumed α_{CO} on the other tracers. We discuss two hypotheses: ULIRG-like value (0.8, Downes & Solomon 1998; Engel et al. 2010) and Milky

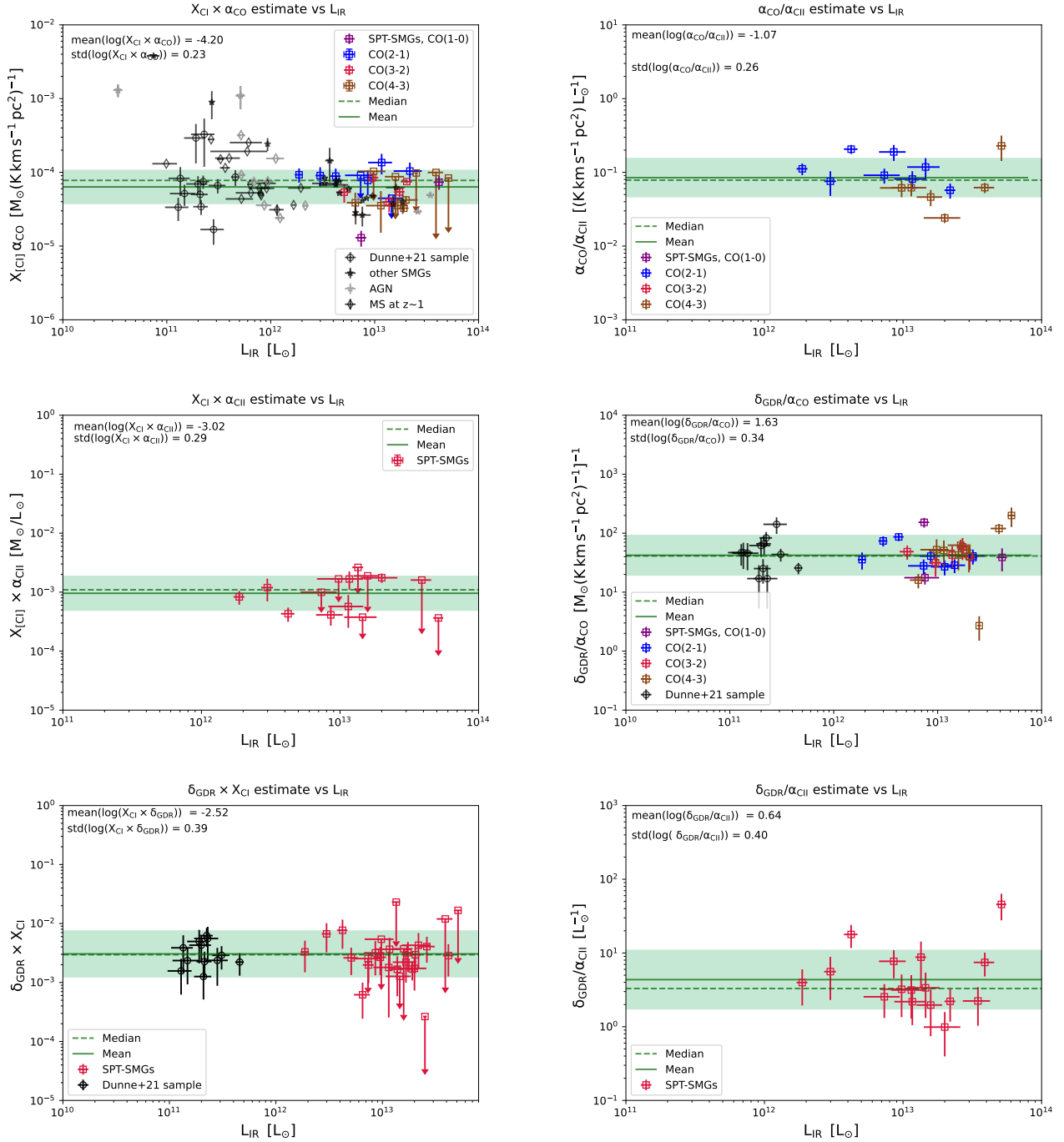


Fig. 6. $X_{\text{CI}} \times \alpha_{\text{CO}}$, $X_{\text{CI}} \times \alpha_{\text{CII}}$, and $X_{\text{CI}} \times \delta_{\text{GDR}}$ (left column) and $\alpha_{\text{CO}}/\alpha_{\text{CII}}$, $\delta_{\text{GDR}}/\alpha_{\text{CO}}$, and $\delta_{\text{GDR}}/\alpha_{\text{CII}}$ (right column) as a function of L_{IR} for our sample. Our sample is represented in squares, colour-coded by the CO transition used to estimate the CO-based gas mass: CO(1–0) transition in purple, CO(2–1) in blue, CO(3–2) in red, and CO(4–3) in brown (top and centre rows). We also compare our sample with the sample presented in Dunne et al. (2021) (black circles), SMGs (black stars), main-sequence galaxies at $z \sim 1$ (black diamonds), and AGNs (grey diamonds) from the Valentino et al. (2020) compilation. The mean and the median y values are shown as green solid and dashed lines, respectively, in the left panel. The green shaded region represents the 1σ region around the sample mean.

Way-like value (3.4, Papadopoulos et al. 2012; Bolatto et al. 2013; Harrington et al. 2021; Jarugula et al. 2021).

Assuming an $\alpha_{\text{CO}} = 3.4$, we can compute a value of $X_{\text{CI}} = 1.86 \pm 0.20 \times 10^{-5}$. The value of X_{CI} is lower than the commonly adopted value of $X_{\text{CI}} = 3 \times 10^{-5}$ (e.g., Papadopoulos et al. 2004; Bothwell et al. 2017). However, it is in agreement with [CI] abundance found in the Milky Way (Frerking et al. 1989), in the sample presented in Dunne et al.

2021 ($X_{\text{CI}} = (1.6 \pm 0.3) \times 10^{-5}$), and in the main-sequence galaxies presented in Valentino et al. 2018 ($1.6\text{--}1.9 \times 10^{-5}$).

We find a corresponding value of $\delta_{\text{GDR}} = 145 \pm 22$ with $\alpha_{\text{CO}} = 3.4$, and it is higher than the commonly adopted value of $\delta_{\text{GDR}} = 100$ for massive galaxies with near-solar metallicities (e.g., Leroy et al. 2011; Rémy-Ruyer et al. 2014). Zavala et al. (2022) also found a similar value of $\delta_{\text{GDR}} = 105 \pm 40$ for a massive compact DSFG at $z = 6$. The high δ_{GDR} value of our sample

Table 4. Mean value of the cross-calibration of gas mass tracers.

Cross-calibration of tracers	Value
$X_{\text{CI}} \times \alpha_{\text{CO}} (\times 10^{-5})$	6.31 ± 0.67
$X_{\text{CI}} \times \alpha_{[\text{CII}]} (\times 10^{-5})$	95.5 ± 17.1
$X_{\text{CI}} \times \delta_{\text{GDR}} (\times 10^{-5})$	302.0 ± 52.2
$\alpha_{\text{CO}}/\alpha_{[\text{CII}]}$	0.08 ± 0.01
$\delta_{\text{GDR}}/\alpha_{\text{CO}}$	42.66 ± 6.43
$\delta_{\text{GDR}}/\alpha_{[\text{CII}]}$	4.36 ± 1.07

Notes. The mean value was estimated using Linmix, which accounts for errors and upper limits.

is in better agreement with the $\delta_{\text{GDR}} = 129 \pm 57$ presented for the Dunne et al. (2021) sample. With an $\alpha_{\text{CO}} = 3.4$, we find a corresponding value of $\alpha_{[\text{CII}]} = 40 \pm 6 M_{\odot}/L_{\odot}$. This is higher than the values calibrated in Zanella et al. (2018), $\alpha_{[\text{CII}]} = 30 M_{\odot}/L_{\odot}$, but is compatible at a 2σ level.

Assuming an $\alpha_{\text{CO}} = 0.8$, we can compute a higher value of $X_{\text{CI}} = 7.9 \pm 0.80 \times 10^{-5}$. Similar values are adopted in Walter et al. (2011) for a sample of Quasi Stellar Objects (QSOs) and they adopt an $\alpha_{\text{CO}} = 0.8$ to derive the X_{CI} values. There are some plausible explanations for these X_{CI} values in the literature. Izumi et al. (2020) find a similarly high value of $X_{\text{CI}} \sim 7 \times 10^{-5}$. They suggest that these high [CI] abundances could result from an X-ray dominated region (XDR) of the ISM. The higher values of X_{CI} can be found in denser regions (e.g., Bisbas et al. 2021) and/or with higher metallicities (e.g., Heintz & Watson 2020). Additionally, the destruction of CO due to far-UV photons in regions of high star formation can further increase the [CI] abundances (e.g., Bisbas et al. 2021).

With this value, we derive a low $\delta_{\text{GDR}} = 34 \pm 5$ for our sample. A higher gas phase metallicity can also lead to low gas-to-dust ratios (e.g., Hunt et al. 2005; Leroy et al. 2011; Saintonge et al. 2013; Popping & Péroux 2022; Popping et al. 2023). Thus, if our sample was dominated by super-solar metallicity galaxies (e.g., galaxies presented in De Breuck et al. 2019; Litke et al. 2023), such low values of δ_{GDR} could be plausible. Using the models from Popping et al. (2017), on the gas-to-dust ratio and metallicity relation we obtain a $\delta_{\text{GDR}} \sim 300$ for a galaxy with solar metallicity at $z \sim 4$ (as seen in De Breuck et al. 2019). Although the model demonstrates a decreasing δ_{GDR} with increasing metallicities, the predicted δ_{GDR} remains high. This could arise from the model being inefficient in reproducing the dust production from metals at high z . We find similar values to those in the observations of Popping et al. (2023), $\delta_{\text{GDR}} \sim 400$. This value also includes the contribution of atomic hydrogen gas and is estimated using quasar absorption sightlines through the neutral ISM. These differences in methodology and selection could contribute to the much higher δ_{GDR} found in that work. In the near future we should be able to probe the dependencies of the carbon abundance (X_{CI}) and δ_{GDR} on the metallicity with JWST.

Using an α_{CO} value of 0.8, we derive a low $\alpha_{[\text{CII}]} = 9.4 \pm 1.5 M_{\odot}/L_{\odot}$. This value is compatible with the $\alpha_{[\text{CII}]} = 7^{+4}_{-1} M_{\odot}/L_{\odot}$ reported by Rizzo et al. (2021) for a sample of five SPT-SMGs. Vizgan et al. (2022) estimated the $\alpha_{[\text{CII}]}$ values for a simulated sample of galaxies and found a median value of $\alpha_{[\text{CII}]} = 18 M_{\odot}/L_{\odot}$ with a median absolute deviation of $10 M_{\odot}/L_{\odot}$. This is slightly higher than the $\alpha_{[\text{CII}]}$ values we derive with a ULIRG-like α_{CO} . They also find that the $\alpha_{[\text{CII}]}$ values can depend on the mass of the system with lower values predicted for more massive galaxies ($M^* > 10^9 M_{\odot}$). Additionally, they find the peak of the

$\alpha_{[\text{CII}]}$ distribution for their sample at $\sim 15 M_{\odot}/L_{\odot}$ and find many galaxies with $\alpha_{[\text{CII}]} < 10 M_{\odot}/L_{\odot}$. Sommovigo et al. (2021) find a variation in $\alpha_{[\text{CII}]}$ between normal star-forming galaxies and starbursts ($\lesssim 10 M_{\odot}/L_{\odot} \alpha_{[\text{CII}]}$ in starbursts).

Additional constraints, such as dynamical mass estimates and metallicity, can help get a better estimate of the absolute values of these tracers. Comparing the gas mass estimates with the dynamical mass can help us predict the values of these tracers (e.g., Bertemes et al. 2018; Zavala et al. 2022; Gururajan et al. 2022); however, such data are available only for a small number of sources. We also make an important assumption that all these tracers trace the same region of molecular gas content of the galaxy, which has been debated in the literature.

In Fig. 6 we do not see a trend with L_{IR} for the various tracers. However, on the y -axis we compare either a product or ratio of these tracers with L_{IR} . In this scenario we may miss a systematic effect with L_{IR} if the tracers have an opposite (product) or similar (ratio) trend with L_{IR} , and compensate each other. This can also be interpreted as a counter argument, that is, if one of the tracers is shown to not have a trend with L_{IR} , then the other two tracers will also have no systematic effect versus L_{IR} .

We discuss the possibilities of two values of α_{CO} and their implications on X_{CI} and δ_{GDR} in the above section. A third scenario could be the possibility of α_{CO} varying with L_{IR} , such that α_{CO} decreases from 3.4 at low L_{IR} to 0.8 at high L_{IR} . Since we do not see a trend with L_{IR} in Fig. 6, this could imply that X_{CI} , δ_{GDR} , and $\alpha_{[\text{CII}]}$ should vary by the same factor in the following range of IR luminosities. A variation of the same factor in all four tracers is unlikely, and thus the various gas tracers are not likely to have a significant trend with L_{IR} .

6.3. Depletion timescales

We finally compute the depletion timescale (t_{dep}) of our sample as $M_{\text{gas}}/\text{SFR}$ [Gyr]. We use the gas mass estimated with CO line using an $\alpha_{\text{CO}} = 3.4$ and find a mean t_{dep} of 212 ± 26 Myr with a range of 63.3–603.9 Myr for our sample. We also compute the depletion timescale with a lower $\alpha_{\text{CO}} = 0.8$ and find a mean depletion time to 49.75 ± 6.07 Myr and the range varying from 14.9–142.1 Myr. In Fig. 7 we plot the evolution of depletion time with redshift z for our sample, along with the SMGs in literature (Carilli et al. 2010; Walter et al. 2012; Ivison et al. 2013; Fu et al. 2012, 2013; Alaghband-Zadeh et al. 2013). The grey shaded region represents the depletion timescale evolution with redshift for main-sequence galaxies from Saintonge et al. (2013), $t_{\text{dep}} = 1.5(1+z)^{\alpha}$, where α varies from -1.5 (Davé et al. 2012) to -1.0 (Magnelli et al. 2013).

We do not see a clear trend in the evolution of t_{dep} with z for our sample unlike the main sequence. With $\alpha_{\text{CO}} = 3.4$, our sample has a depletion timescale similar to the main sequence at the redshift range, with 8/29 sources having shorter depletion times than the main sequence, and 3/29 sources having longer depletion times than the main sequence. Although these sources have a high SFR, their depletion time is similar to that of main-sequence galaxies. This could be a hint towards these systems having a large gas reservoir (e.g., Tacconi et al. 2010; Daddi et al. 2010a; Saintonge et al. 2013; Dessauges-Zavadsky et al. 2015; Béthermin et al. 2015) with rapid accretion of cold gas from the cosmic web (e.g., Dekel et al. 2009; Kleiner et al. 2017; Kretschmer et al. 2020; Chun et al. 2020). However, if we adopt a lower value of $\alpha_{\text{CO}} = 0.8$, these objects would fall far below the main sequence with a short depletion timescale.

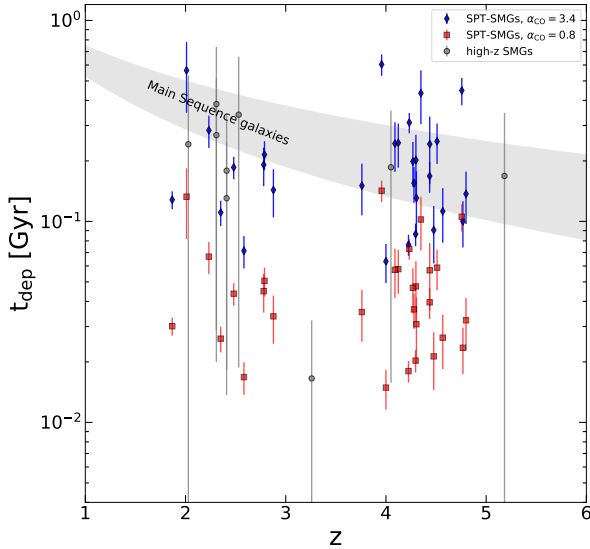


Fig. 7. Depletion timescale as a function of redshift for our sample. We compare the depletion timescale of our sample (blue diamonds and red squares) along with the SMGs (grey circles) from Carilli et al. (2010), Walter et al. (2012), Ivison et al. (2013), Fu et al. (2012, 2013), Alaghband-Zadeh et al. (2013). The blue diamonds represent the depletion timescales corresponding to gas mass calculated using $\alpha_{\text{CO}} = 3.4$ and the red squares are computed using $\alpha_{\text{CO}} = 0.8$. The main sequence in the grey shaded region follows the relation presented in Saintonge et al. (2013), with α values ranging from -1.5 (Davé et al. 2012) to -1.0 (Magnelli et al. 2013).

7. Summary and conclusions

We present a sample of 29 DSFGs in the redshift range 1.867–4.799 and the flux catalogue of [CI](1–0), [CI](2–1), and [CII] lines for these galaxies, combining the ancillary observations presented in Bothwell et al. (2017), Reuter et al. (2020), and Gullberg et al. (2015). The main conclusions of the work are presented below:

- We compare the IR luminosity to the [CI] luminosity of our sample. This is a proxy for the integrated Kennicutt-Schmidt law, with the L_{IR} tracing the SFR and L_{CI} tracing the gas mass. In the case of L_{IR} versus $L_{\text{[CI](1-0)}}$, we find that the slope of the relation for our sample is in agreement with the L_{FIR} versus $L'_{\text{CO(1-0)}}$ slopes presented in Greve et al. (2014), Liu et al. (2015) and Kamenetzky et al. (2016). On combining our sample with local galaxies, main-sequence galaxies, and other SMGs, we find a super-linear relation, suggesting that there may be a different trend between the starbursting SMGs and the local-main-sequence sample (Daddi et al. 2010b; Genzel et al. 2010). The relation between [CI](2–1) and IR luminosity does not show a difference in slope for SMGs and local-main-sequence galaxies which could be attributed to a higher excitation of [CI](2–1) in starbursts.
- Comparing the $L_{\text{[CI](1-0)}}/L_{\text{CO(4-3)}}$ and $L_{\text{[CI](1-0)}}/L_{\text{IR}}$ ratios of our sample with the compilation presented in Valentino et al. (2020), we find that our sample has comparable densities and radiation field intensities to the other SMGs. In comparison with the main-sequence and the local galaxies, they have higher intensities, but with a strong overlap.
- We compute the [CI] excitation temperature for our sample, and it is in the range 17.7–64.2 K with a mean sample value of 34.5 ± 2.1 K. On comparing the [CI] excitation temperatures to the dust temperature, $T_{\text{ex}}/T_{\text{dust}} < 1$. We do not find any candidates for cold and/or optically thick dust.

- Comparing our molecular mass estimates with four tracers, [CI](1–0), CO(1–0), dust, and [CII], we provide a cross-calibration for the uncertain parameters X_{CI} , α_{CO} , δ_{GDR} , and $\alpha_{\text{[CII]}}$. Overall, there is good agreement between all these tracers and the scatter between α_{CO} , X_{CI} , δ_{GDR} , and $\alpha_{\text{[CII]}}$ (Fig. 6) can be reproduced by measurement uncertainties.
- Higher values of α_{CO} , (~ 3.4) predict a lower [CI]-abundance, a higher dust-to-gas ratio, and a value of [CII]-to- H_2 conversion factor similar to that found by Zanella et al. (2018). This could be possible in low-metallicity regimes. ULIRG-like values of α_{CO} give a higher [CI] abundance and a low $\alpha_{\text{[CII]}}$ and very low δ_{GDR} , which can be the case for metal-rich systems.

To summarise, we estimate the molecular gas mass of our sample using various molecular gas tracers such as CO, [CI], [CII], and dust. These tracers are consistent and show an agreement with one another. We cross-calibrate the uncertain factors such as X_{CI} , α_{CO} , $\alpha_{\text{[CII]}}$, and δ_{GDR} .

Acknowledgements. We thank Francesco Valentino for providing the data associated with his [CI] data compilation. We thank the referee for their valuable comments. ALMA is a partnership of ESO (representing its member states), NSF (USA) and NINS (Japan), together with NRC (Canada), MOST and ASIAA (Taiwan) and KASI (Republic of Korea), in cooperation with the Republic of Chile. The Joint ALMA Observatory is operated by ESO, AUI/NRAO and NAOJ. The National Radio Astronomy Observatory is a facility of the National Science Foundation operated under cooperative agreement by Associated Universities, Inc. This publication is based on data acquired with the Atacama Pathfinder Experiment (APEX). APEX is a collaboration between the Max-Planck-Institut für Radioastronomie, the European Southern Observatory and the Onsala Space Observatory. Based on observations made with ESO Telescopes at the La Silla Paranal Observatory under programme ID 097.A-0973. This work was supported by the Programme National “Physique et Chimie du Milieu Interstellaire” (PCMI) of CNRS/INSU with INC/INP co-funded by CEA and CNES. This work was supported by the Programme National Cosmologie et Galaxies (PNCG) of CNRS/INSU with INP and IN2P3, co-funded by CEA and CNES. GG acknowledges support from the grants PRIN MIUR 2017 – 20173ML3WW_001, ASI n.1/023/12/0 and INAF-PRIN 1.05.01.85.08. MA acknowledges support from FONDECYT grant 1211951, ANID+PCI+INSTITUTO MAX PLANCK DE ASTRONOMIA MPG 190030, ANID+PCI+REDES 190194 and ANID BASAL project FB210003. TRG acknowledges support from the Carlsberg Foundation (grant no CF20-0534). The Cosmic Dawn Center (DAWN) is funded by the Danish National Research Foundation under grant No. 140.

References

- Abdo, A. A., Ackermann, M., Ajello, M., et al. 2010, *ApJ*, **710**, 133
- Alaghband-Zadeh, S., Chapman, S. C., Swinbank, A. M., et al. 2013, *MNRAS*, **435**, 1493
- Allen, R. J., Ivette Rodríguez, M., Black, J. H., & Booth, R. S. 2012, *AJ*, **143**, 97
- Andreani, P., Retana-Montenegro, E., Zhang, Z.-Y., et al. 2018, *A&A*, **615**, A142
- Aravena, M., Spilker, J. S., Bethermin, M., et al. 2016, *MNRAS*, **457**, 4406
- Bertemes, C., Wuyts, S., Lutz, D., et al. 2018, *MNRAS*, **478**, 1442
- Bethermin, M., Daddi, E., Magdis, G., et al. 2015, *A&A*, **573**, A113
- Bisbas, T. G., Papadopoulos, P. P., & Viti, S. 2015, *ApJ*, **803**, 37
- Bisbas, T. G., Tan, J. C., & Tanaka, K. E. I. 2021, *MNRAS*, **502**, 2701
- Bisbas, T. G., van Dishoeck, E. F., Papadopoulos, P. P., et al. 2017, *ApJ*, **839**, 90
- Bolatto, A. D., Wolfire, M., & Leroy, A. K. 2013, *ARA&A*, **51**, 207
- Bothwell, M. S., Aguirre, J. E., Aravena, M., et al. 2017, *MNRAS*, **466**, 2825
- Bourne, N., Dunlop, J. S., Simpson, J. M., et al. 2019, *MNRAS*, **482**, 3135
- Calistro Rivera, G., Hodge, J. A., Smail, I., et al. 2018, *ApJ*, **863**, 56
- Cañameras, R., Nesvadba, N. P. H., Guery, D., et al. 2015, *A&A*, **581**, A105
- Cañameras, R., Yang, C., Nesvadba, N. P. H., et al. 2018, *A&A*, **620**, A61
- Capak, P. L., Carilli, C., Jones, G., et al. 2015, *Nature*, **522**, 455
- Carilli, C. L., & Walter, F. 2013, *ARA&A*, **51**, 105
- Carilli, C. L., Daddi, E., Riechers, D., et al. 2010, *ApJ*, **714**, 1407
- Casey, C. M., Narayanan, D., & Cooray, A. 2014, *Phys. Rep.*, **541**, 45
- Chabrier, G. 2003, *PASP*, **115**, 763
- Chun, K., Smith, R., Shin, J., Kim, S. S., & Raouf, M. 2020, *ApJ*, **889**, 173
- Conway, J. E., Cornwell, T. J., & Wilkinson, P. N. 1990, *MNRAS*, **246**, 490
- Cormier, D., Madden, S. C., Lebouteiller, V., et al. 2015, *A&A*, **578**, A53
- Cortzen, I., Magdis, G. E., Valentino, F., et al. 2020, *A&A*, **634**, L14
- Croxall, K. V., Smith, J. D., Pellegrini, E., et al. 2017, *ApJ*, **845**, 96
- da Cunha, E., Walter, F., Decarli, R., et al. 2013, *ApJ*, **765**, 9
- Daddi, E., Bournaud, F., Walter, F., et al. 2010a, *ApJ*, **713**, 686

- Daddi, E., Elbaz, D., Walter, F., et al. 2010b, *ApJ*, **714**, L118
- Daddi, E., Dannerbauer, H., Liu, D., et al. 2015, *A&A*, **577**, A46
- Dannerbauer, H., Harrington, K., Díaz-Sánchez, A., et al. 2019, *AJ*, **158**, 34
- Davé, R., Finlator, K., & Oppenheimer, B. D. 2012, *MNRAS*, **421**, 98
- De Breuck, C., Weiß, A., Béthermin, M., et al. 2019, *A&A*, **631**, A167
- Decarli, R., Aravena, M., Boogaard, L., et al. 2020, *ApJ*, **902**, 110
- Dekel, A., Birnboim, Y., Engel, G., et al. 2009, *Nature*, **457**, 451
- Dessauges-Zavadsky, M., Zamojski, M., Schaerer, D., et al. 2015, *A&A*, **577**, A50
- Dessauges-Zavadsky, M., Ginolfi, M., Pozzi, F., et al. 2020, *A&A*, **643**, A5
- Díaz-Santos, T., Armus, L., Charmandaris, V., et al. 2017, *ApJ*, **846**, 32
- Downes, D., & Solomon, P. M. 1998, *ApJ*, **507**, 615
- Dunne, L., Maddox, S. J., Vlahakis, C., & Gomez, H. L. 2021, *MNRAS*, **501**, 2573
- Dunne, L., Maddox, S. J., Papadopoulos, P. P., Ivison, R. J., & Gomez, H. L. 2022, *MNRAS*, **517**, 962
- Eales, S., Smith, M. W. L., Auld, R., et al. 2012, *ApJ*, **761**, 168
- Engel, H., Tacconi, L. J., Davies, R. I., et al. 2010, *ApJ*, **724**, 233
- Feldmann, R., Gnedin, N. Y., & Kravtsov, A. V. 2012, *ApJ*, **747**, 124
- Frerking, M. A., Keene, J., Blake, G. A., & Phillips, T. G. 1989, *ApJ*, **344**, 311
- Fu, H., Jullo, E., Cooray, A., et al. 2012, *ApJ*, **753**, 134
- Fu, H., Cooray, A., Feruglio, C., et al. 2013, *Nature*, **498**, 338
- Fudamoto, Y., Oesch, P. A., Faisst, A., et al. 2020, *A&A*, **643**, A4
- Genzel, R., Tacconi, L. J., Gracia-Carpio, J., et al. 2010, *MNRAS*, **407**, 2091
- Genzel, R., Tacconi, L. J., Combes, F., et al. 2012, *ApJ*, **746**, 69
- Glover, S. C. O., & Smith, R. J. 2016, *MNRAS*, **462**, 3011
- Greve, T. R., Leonidaki, I., Xilouris, E. M., et al. 2014, *ApJ*, **794**, 142
- Gullberg, B., De Breuck, C., Vieira, J. D., et al. 2015, *MNRAS*, **449**, 2883
- Gururajan, G., Béthermin, M., Theulé, P., et al. 2022, *A&A*, **663**, A22
- Harrington, K. C., Weiss, A., Yun, M. S., et al. 2021, *ApJ*, **908**, 95
- Heinis, S., Buat, V., Béthermin, M., et al. 2014, *MNRAS*, **437**, 1268
- Heintz, K. E., & Watson, D. 2020, *ApJ*, **889**, L7
- Heyminck, S., Kasemann, C., Güsten, R., de Lange, G., & Graf, U. U. 2006, *A&A*, **454**, L21
- Hopkins, A. M., & Beacom, J. F. 2006, *ApJ*, **651**, 142
- Hughes, T. M., Ibar, E., Villanueva, V., et al. 2017, *A&A*, **602**, A49
- Hunt, L., Bianchi, S., & Maiolino, R. 2005, *A&A*, **434**, 849
- Ikeda, M., Oka, T., Tatematsu, K., Sekimoto, Y., & Yamamoto, S. 2002, *ApJS*, **139**, 467
- Ivison, R. J., Swinbank, A. M., Smail, I., et al. 2013, *ApJ*, **772**, 137
- Izumi, T., Nguyen, D. D., Imanishi, M., et al. 2020, *ApJ*, **898**, 75
- Jarugula, S., Vieira, J. D., Weiss, A., et al. 2021, *ApJ*, **921**, 97
- Jin, S., Daddi, E., Magdis, G. E., et al. 2019, *ApJ*, **887**, 144
- Kamenetzky, J., Rangwala, N., Glenn, J., Maloney, P. R., & Conley, A. 2014, *ApJ*, **795**, 174
- Kamenetzky, J., Rangwala, N., Glenn, J., Maloney, P. R., & Conley, A. 2016, *ApJ*, **829**, 93
- Kaufman, M. J., Wolfire, M. G., Hollenbach, D. J., & Luhman, M. L. 1999, *ApJ*, **527**, 795
- Kaufman, M. J., Wolfire, M. G., & Hollenbach, D. J. 2006, *ApJ*, **644**, 283
- Keene, J., Blake, G. A., Phillips, T. G., Huggins, P. J., & Beichman, C. A. 1985, *ApJ*, **299**, 967
- Kelly, B. C. 2007, *ApJ*, **665**, 1489
- Kennicutt, R. C., Jr. 1998, *ARA&A*, **36**, 189
- Kennicutt, R. C., & Evans, N. J. 2012, *ARA&A*, **50**, 531
- Klein, B., Philipp, S. D., Krämer, I., et al. 2006, *A&A*, **454**, L29
- Kleiner, D., Pimblett, K. A., Jones, D. H., Koribalski, B. S., & Serra, P. 2017, *MNRAS*, **466**, 4692
- Kretschmer, M., Agertz, O., & Teyssier, R. 2020, *MNRAS*, **497**, 4346
- Krumholz, M. R., Leroy, A. K., & McKee, C. F. 2011, *ApJ*, **731**, 25
- Lagos, C. d. P., Bayet, E., Baugh, C. M., et al. 2012, *MNRAS*, **426**, 2142
- Langer, W. 1976, *ApJ*, **206**, 699
- Langer, W. D., Velusamy, T., Pineda, J. L., Willacy, K., & Goldsmith, P. F. 2014, *A&A*, **561**, A122
- Le Floc'h, E., Papovich, C., Dole, H., et al. 2005, *ApJ*, **632**, 169
- Leroy, A. K., Bolatto, A., Gordon, K., et al. 2011, *ApJ*, **737**, 12
- Litke, K. C., Marrone, D. P., Aravena, M., et al. 2023, *ApJ*, **949**, 87
- Liu, D., Gao, Y., Isaak, K., et al. 2015, *ApJ*, **810**, L14
- Ma, J., Gonzalez, A. H., Spilker, J. S., et al. 2015, *ApJ*, **812**, 88
- Madau, P., & Dickinson, M. 2014, *ARA&A*, **52**, 415
- Madau, P., Ferguson, H. C., Dickinson, M. E., et al. 1996, *MNRAS*, **283**, 1388
- Magdis, G. E., Daddi, E., Elbaz, D., et al. 2011, *ApJ*, **740**, L15
- Magnelli, B., Popesso, P., Berta, S., et al. 2013, *A&A*, **553**, A132
- Maloney, P. R., & Wolfire, M. G. 1997, *IAU Symposium*, **170**, 299
- McMullin, J. P., Waters, B., Schiebel, D., Young, W., & Golap, K. 2007, in *Astronomical Data Analysis Software and Systems XVI*, eds. R. A. Shaw, F. Hill, & D. J. Bell, *ASP Conf. Ser.*, **376**, 127
- Murphy, E. J., Condon, J. J., Schinnerer, E., et al. 2011, *ApJ*, **737**, 67
- Narayanan, D., & Krumholz, M. R. 2014, *MNRAS*, **442**, 1411
- Narayanan, D., Krumholz, M., Ostriker, E. C., & Hernquist, L. 2011, *MNRAS*, **418**, 664
- Narayanan, D., Krumholz, M. R., Ostriker, E. C., & Hernquist, L. 2012, *MNRAS*, **421**, 3127
- Nesvadba, N. P. H., Cañameras, R., Kneissl, R., et al. 2019, *A&A*, **624**, A23
- Ojha, R., Stark, A. A., Hsieh, H. H., et al. 2001, *ApJ*, **548**, 253
- Oka, T., Hasegawa, T., Hayashi, M., Handa, T., & Sakamoto, S. 1998, *ApJ*, **493**, 730
- Papadopoulos, P. P., & Greve, T. R. 2004, *ApJ*, **615**, L29
- Papadopoulos, P. P., Thi, W. F., & Viti, S. 2004, *MNRAS*, **351**, 147
- Papadopoulos, P. P., van der Werf, P. P., Xilouris, E. M., et al. 2012, *MNRAS*, **426**, 2601
- Papadopoulos, P., Dunne, L., & Maddox, S. 2022, *MNRAS*, **510**, 725
- Pérez-Beaupuits, J. P., Stutzki, J., Ossenkopf, V., et al. 2015, *A&A*, **575**, A9
- Pineda, J. L., Langer, W. D., Velusamy, T., & Goldsmith, P. F. 2013, *A&A*, **554**, A103
- Pineda, J. L., Langer, W. D., & Goldsmith, P. F. 2014, *A&A*, **570**, A121
- Pineda, J. L., Langer, W. D., Goldsmith, P. F., et al. 2017, *ApJ*, **839**, 107
- Plume, R., Jaffe, D. T., Tatematsu, K., Evans, Neal J., & I., & Keene, 1999, *J. ApJ*, **512**, 768
- Popping, G., & Péroux, C. 2022, *MNRAS*, **513**, 1531
- Popping, G., Somerville, R. S., & Galametz, M. 2017, *MNRAS*, **471**, 3152
- Popping, G., Narayanan, D., Somerville, R. S., Faisst, A. L., & Krumholz, M. R. 2019, *MNRAS*, **482**, 4906
- Popping, G., Shivaee, I., Sanders, R. L., et al. 2023, *A&A*, **670**, A138
- Pound, M. W., & Wolfire, M. G. 2023, *AJ*, **165**, 25
- Rémy-Ruyer, A., Madden, S. C., Galliano, F., et al. 2014, *A&A*, **563**, A31
- Reuter, C., Vieira, J. D., Spilker, J. S., et al. 2020, *ApJ*, **902**, 78
- Rigopoulou, D., Hopwood, R., Magdis, G. E., et al. 2014, *ApJ*, **781**, L15
- Rizzo, F., Vegetti, S., Fraternali, F., Stacey, H. R., & Powell, D. 2021, *MNRAS*, **507**, 3952
- Saintonge, A., Lutz, D., Genzel, R., et al. 2013, *ApJ*, **778**, 2
- Sandstrom, K. M., Leroy, A. K., Walter, F., et al. 2013, *ApJ*, **777**, 5
- Sargent, M. T., Béthermin, M., Daddi, E., & Elbaz, D. 2012, *ApJ*, **747**, L31
- Sargsyan, L., Lebouteiller, V., Weedman, D., et al. 2012, *ApJ*, **755**, 171
- Schneider, N., Simon, R., Kramer, C., et al. 2003, *A&A*, **406**, 915
- Schruba, A., Leroy, A. K., Walter, F., et al. 2012, *AJ*, **143**, 138
- Scoville, N., Aussel, H., Sheth, K., et al. 2014, *ApJ*, **783**, 84
- Scoville, N., Sheth, K., Aussel, H., et al. 2016, *ApJ*, **820**, 83
- Shetty, R., Glover, S. C., Dullemond, C. P., et al. 2011, *MNRAS*, **415**, 3253
- Shi, Y., Wang, J., Zhang, Z.-Y., et al. 2015, *ApJ*, **804**, L11
- Shi, Y., Wang, J., Zhang, Z.-Y., et al. 2016, *Nat. Commun.*, **7**, 13789
- Smith, R. J., Glover, S. C. O., Clark, P. C., Klessen, R. S., & Springel, V. 2014, *MNRAS*, **441**, 1628
- Solomon, P. M., & Vanden Bout, P. A. 2005, *ARA&A*, **43**, 677
- Solomon, P. M., Rivolo, A. R., Barrett, J., & Yahil, A. 1987, *ApJ*, **319**, 730
- Sommovigo, L., Ferrara, A., Carniani, S., et al. 2021, *MNRAS*, **503**, 4878
- Spilker, J. S., Marrone, D. P., Aguirre, J. E., et al. 2014, *ApJ*, **785**, 149
- Spilker, J. S., Aravena, M., Marrone, D. P., et al. 2015, *ApJ*, **811**, 124
- Spilker, J. S., Marrone, D. P., Aravena, M., et al. 2016, *ApJ*, **826**, 112
- Stacey, G. J., Geis, N., Genzel, R., et al. 1991, *ApJ*, **373**, 423
- Strandet, M. L., Weiss, A., Vieira, J. D., et al. 2016, *ApJ*, **822**, 80
- Strong, A. W., & Mattox, J. R. 1996, *A&A*, **308**, L21
- Strong, A. W., Moskalenko, I. V., Reimer, O., Digel, S., & Diehl, R. 2004, *A&A*, **422**, L47
- Stutzki, J., Graf, U. U., Haas, S., et al. 1997, *ApJ*, **477**, L33
- Tacconi, L. J., Genzel, R., Neri, R., et al. 2010, *Nature*, **463**, 781
- Tielens, A. G. G. M., & Hollenbach, D. 1985, *ApJ*, **291**, 722
- Tomassetti, M., Porciani, C., Romano-Díaz, E., Ludlow, A. D., & Papadopoulos, P. P. 2014, *MNRAS*, **445**, L124
- Tunnard, R., & Greve, T. R. 2016, *ApJ*, **819**, 161
- Valentino, F., Magdis, G. E., Daddi, E., et al. 2018, *ApJ*, **869**, 27
- Valentino, F., Magdis, G. E., Daddi, E., et al. 2020, *ApJ*, **890**, 24
- Vallini, L., Gallerani, S., Ferrara, A., Pallottini, A., & Yue, B. 2015, *ApJ*, **813**, 36
- Velusamy, T., & Langer, W. D. 2014, *A&A*, **572**, A45
- Véron-Cetty, M. P., & Véron, P. 2010, *A&A*, **518**, A10
- Vieira, J. D., Marrone, D. P., Chapman, S. C., et al. 2013, *Nature*, **495**, 344
- Vizgan, D., Greve, T. R., Olsen, K. P., et al. 2022, *ApJ*, **929**, 92
- Walter, F., Weiß, A., Downes, D., Decarli, R., & Henkel, C. 2011, *ApJ*, **730**, 18
- Walter, F., Decarli, R., Carilli, C., et al. 2012, *ApJ*, **752**, 93
- Weiß, A., Henkel, C., Downes, D., & Walter, F. 2003, *A&A*, **409**, L41
- Weiß, A., Downes, D., Neri, R., et al. 2007, *A&A*, **467**, 955
- Weiß, A., De Breuck, C., Marrone, D. P., et al. 2013, *ApJ*, **767**, 88
- Wolfire, M. G., Hollenbach, D., & McKee, C. F. 2010, *ApJ*, **716**, 1191
- Yang, C., Omont, A., Beelen, A., et al. 2017, *A&A*, **608**, A144
- Zanella, A., Daddi, E., Magdis, G., et al. 2018, *MNRAS*, **481**, 1976
- Zavala, J. A., Casey, C. M., Spilker, J., et al. 2022, *ApJ*, **933**, 242

Appendix A: Gas mass tracers versus dust temperatures

We compare the cross-calibration relations $X_{\text{Cl}} \times \alpha_{\text{CO}}$, $X_{\text{Cl}} \times \alpha_{[\text{ClI}]}$, $X_{\text{Cl}} \times \delta_{\text{GDR}}$, $\alpha_{\text{CO}}/\alpha_{[\text{ClI}]}$, $\delta_{\text{GDR}}/\alpha_{\text{CO}}$, and $\delta_{\text{GDR}}/\alpha_{[\text{ClI}]}$ with

the dust temperature for our sample. Overall, we do not find a significant trend ($> 3\sigma$) for these tracers. The mild trend ($\sim 2.5\sigma$) we find for $\delta_{\text{GDR}}/\alpha_{\text{CO}}$ could be linked to the $T_{\text{dust}} - M_{\text{dust}}$ degeneracy in the SED fitting.

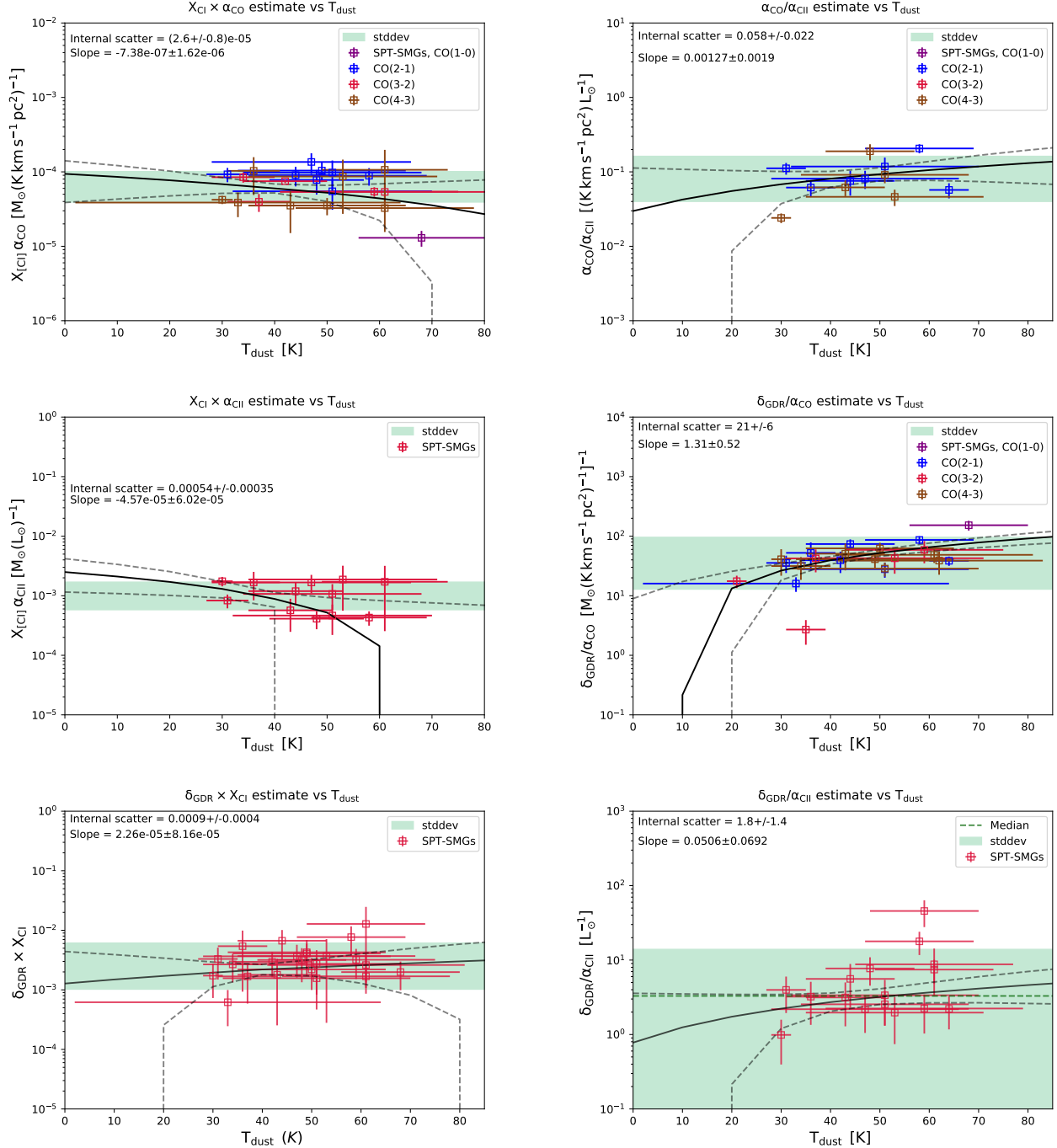


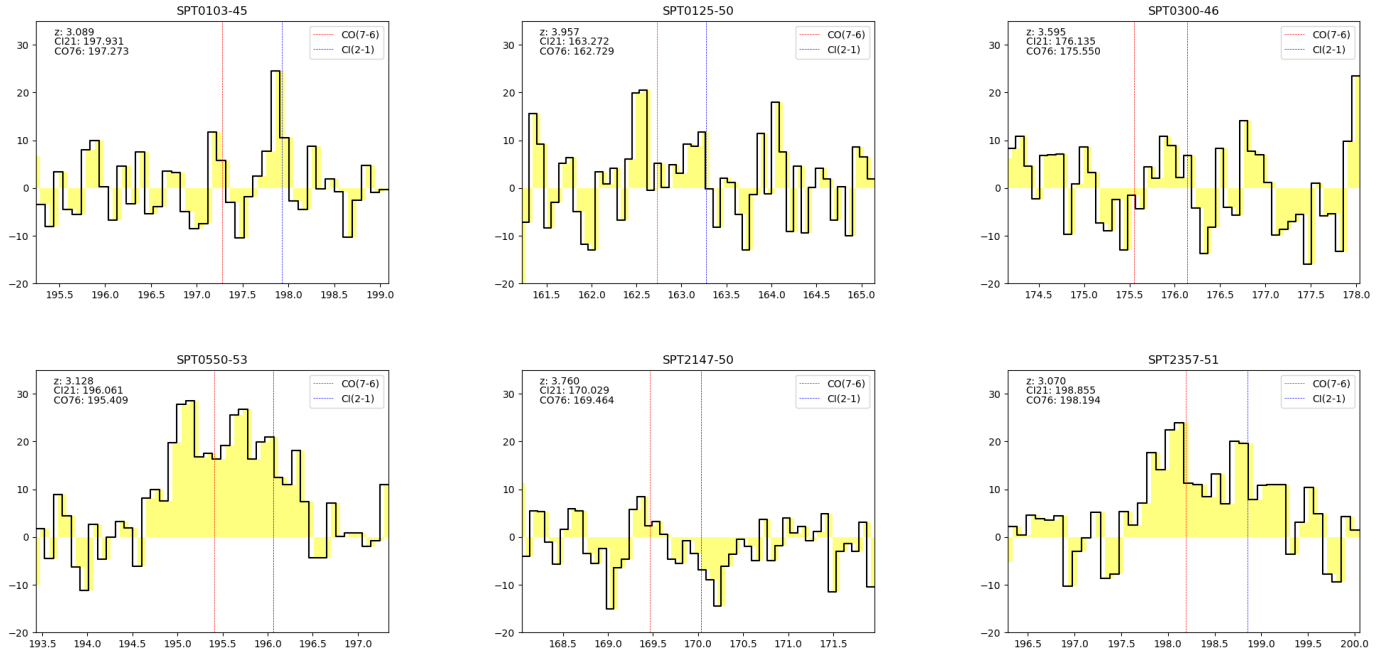
Fig. A.1. $X_{\text{Cl}} \times \alpha_{\text{CO}}$, $X_{\text{Cl}} \times \alpha_{[\text{ClI}]}$, and $X_{\text{Cl}} \times \delta_{\text{GDR}}$ (left column) and $\alpha_{\text{CO}}/\alpha_{[\text{ClI}]}$, $\delta_{\text{GDR}}/\alpha_{\text{CO}}$, and $\delta_{\text{GDR}}/\alpha_{[\text{ClI}]}$ (right column) as a function of T_{dust} for our sample. Our sample is represented in squares, colour-coded by the CO transition used to estimate the CO-based gas mass: CO(1-0) transition in purple, CO(2-1) in blue, CO(3-2) in red, and CO(4-3) in brown (top and centre rows). The green shaded region represents the 1σ region around the sample mean. We also plot the linear regression best fit and the 1σ region from Linmix as the black solid and black-dashed line, respectively.

Table A.1. Slope, intercept, and scatter from the cross-calibration relation

Data	Slope	Intercept	Scatter
Versus L_{IR}			
$\log(X_{\text{CI}} \times \alpha_{\text{CO}})$	-0.04 ± 0.17	-5.59 ± 2.22	0.23 ± 0.05
$\log(X_{\text{CI}} \times \alpha_{[\text{CII}]})$	0.11 ± 0.27	-4.4 ± 3.6	0.29 ± 0.13
$\log(X_{\text{CI}} \times \delta_{\text{GDR}})$	-0.02 ± 0.21	-2.23 ± 2.78	0.39 ± 0.09
$\log(\alpha_{\text{CO}} / \alpha_{[\text{CII}]})$	-0.16 ± 0.24	1.1 ± 3.1	0.26 ± 1.0
$\log(\delta_{\text{GDR}} / \alpha_{\text{CO}})$	0.04 ± 0.21	1.1 ± 2.8	0.34 ± 0.07
$\log(\delta_{\text{GDR}} / \alpha_{[\text{CII}]})$	0.07 ± 0.34	-0.27 ± 4.55	0.41 ± 0.14
Versus T_{dust}			
$X_{\text{CI}} \times \alpha_{\text{CO}}$	$(-0.74 \pm 1.62) \times 10^{-6}$	$(9.0 \pm 5.4) \times 10^{-5}$	$(2.6 \pm 0.8) \times 10^{-5}$
$X_{\text{CI}} \times \alpha_{[\text{CII}]}$	$(-4.57 \pm 6.02) \times 10^{-5}$	$(2.4 \pm 1.6) \times 10^{-3}$	$(5.4 \pm 3.5) \times 10^{-4}$
$X_{\text{CI}} \times \delta_{\text{GDR}}$	$(2.26 \pm 8.16) \times 10^{-5}$	$(-0.28 \pm 2.8) \times 10^{-3}$	$(9 \pm 4) \times 10^{-4}$
$\alpha_{\text{CO}} / \alpha_{[\text{CII}]}$	$(1.3 \pm 1.9) \times 10^{-3}$	$(3.1 \pm 8.8) \times 10^{-2}$	0.058 ± 0.022
$\delta_{\text{GDR}} / \alpha_{\text{CO}}$	1.31 ± 0.52	-12.6 ± 22.6	21 ± 6
$\delta_{\text{GDR}} / \alpha_{[\text{CII}]}$	0.05 ± 0.06	0.82 ± 3.24	1.8 ± 1.4

Appendix B: APEX Spectra

The spectra of our APEX observations of the sources are shown in Fig. B.1.

**Fig. B.1.** Spectra of the APEX sample. The red dotted line indicates the CO(7-6) line and the blue dotted line indicates the [CI](2-1) line.

Appendix C: Deblending [CI](2-1) and CO(7-6) lines

In Fig. 2 the spectra of sources SPT0155-62 and SPT2037-65 have blended CO(7-6) and [CI](2-1) emission. We use a multiple-Gaussian fit in order to estimate the fraction of flux in the blended region. For SPT0155-62, we fit four Gaussians with six free parameters. For the amplitudes we use two central velocities and two line widths, thereby forcing the same width for each of these lines. We thus use the combined width of these two components for each of these lines as the integration window for the moment-0 maps. We can also compute the integrated flux from our fitting procedure. The line fluxes of CO(7-6) and [CI](2-1) estimated by this method are 12.1 ± 1.9 and 8.9 ± 1.6 Jy km/s. The difference between these fluxes and that estimated by the moment-0 maps is $< 1\sigma$. We use the same model for SPT2037-65 and estimate CO(7-6) flux as 9.1 ± 1.7 Jy km/s and [CI](2-1) as 7.1 ± 1.4 Jy km/s. The difference between the moment map estimated flux is $< 1.2\sigma$ for this source. Hence we proceed to use the fluxes estimated by the moment-0 map for uniformity.

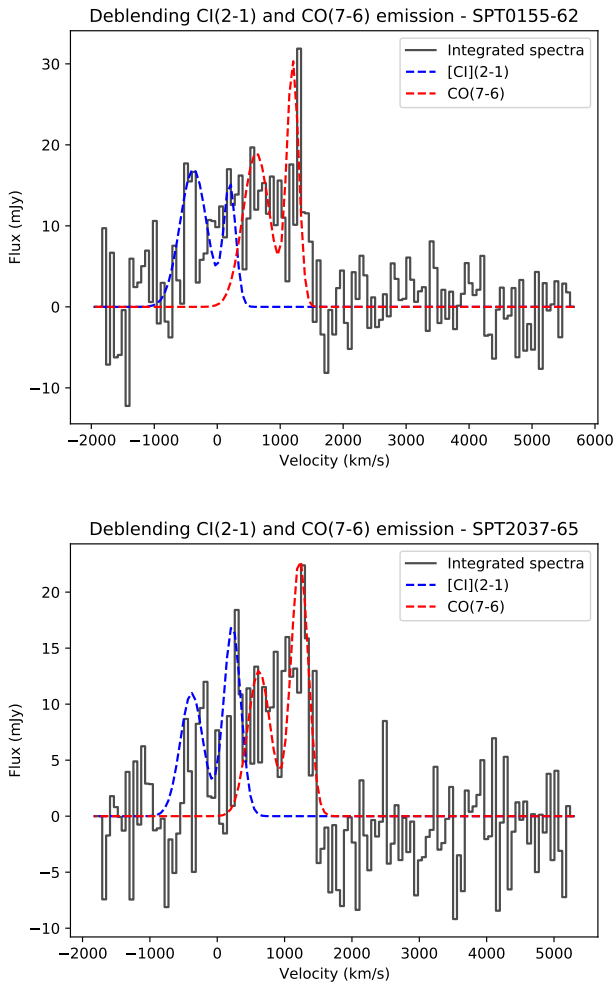


Fig. C.1. Deblending the CO(7-6) and [CI](2-1) lines for sources SPT0155-62 (top panel) and SPT2037-65 (bottom panel). The spectrum is represented by the black solid line. The fit for CO(7-6) is represented as red dashed line and for [CI](2-1) is represented as blue dashed line.

Appendix D: Origin of scatter between various tracers

In Fig. 6 we see a scatter while comparing our tracers with the L_{IR} . Although there is no strong trend and the scatter is less than < 0.41 dex, the factor driving this is unclear. In order to probe the contribution of measurement uncertainties to this scatter, we performed a test to simulate our data with additional uncertainties to see if they could reproduce the scatter.

To do so, we derived a random Gaussian distribution of one of the tracers, example α_{CO} , in terms of another tracer example X_{CI} . In other words, for the $X_{\text{CI}} \times \alpha_{\text{CO}}$ relation against the L_{IR} (Fig. 6, left column, top row), the α_{CO} is traced by the observable quantity, $L'_{\text{CO}(1-0)}$ and X_{CI} is traced by $[1375.8 D_L^2 S_{\nu} \Delta \nu] / [(1+z) Q_{10} A_{10}]$. We generated a random Gaussian for $L'_{\text{CO}(1-0)}$ as a function of the X_{CI} tracer and the median of the $X_{\text{CI}} \times \alpha_{\text{CO}}$ relation. We allowed the sigma of this distribution to be the combined error of the two quantities. This therefore gives us a large array of $L'_{\text{CO}(1-0)}$ values with additional noise. We then use every $L'_{\text{CO}(1-0)}$ value to compute $X_{\text{CI}} \times \alpha_{\text{CO}}$ relation using Eq. 8 for each of our sources.

Table D.1. KS test between the observed data and the simulated data with noise

Data	Deviation	p-Value
$X_{\text{CI}} \times \alpha_{\text{CO}}$	0.18	0.39
$X_{\text{CI}} \times \alpha_{[\text{CI}]}$	0.30	0.13
$X_{\text{CI}} \times \delta_{\text{GDR}}$	0.18	0.35
$\alpha_{\text{CO}} / \alpha_{[\text{CI}]}$	0.21	0.48
$\delta_{\text{GDR}} / \alpha_{\text{CO}}$	0.15	0.50
$\delta_{\text{GDR}} / \alpha_{[\text{CI}]}$	0.32	0.06

In Fig. D we compare the observed ratios between tracers, along with simulated ratios assuming no scatter but including instrumental noise. The KS tests comparing our observed distribution and the simulated distribution (Table D.1) return p-values higher than 0.05 for all the combination of tracers. Thus, we do not find any evidence of intrinsic scatter, which is probably undetected due to our small sample size and the large measurement uncertainties.

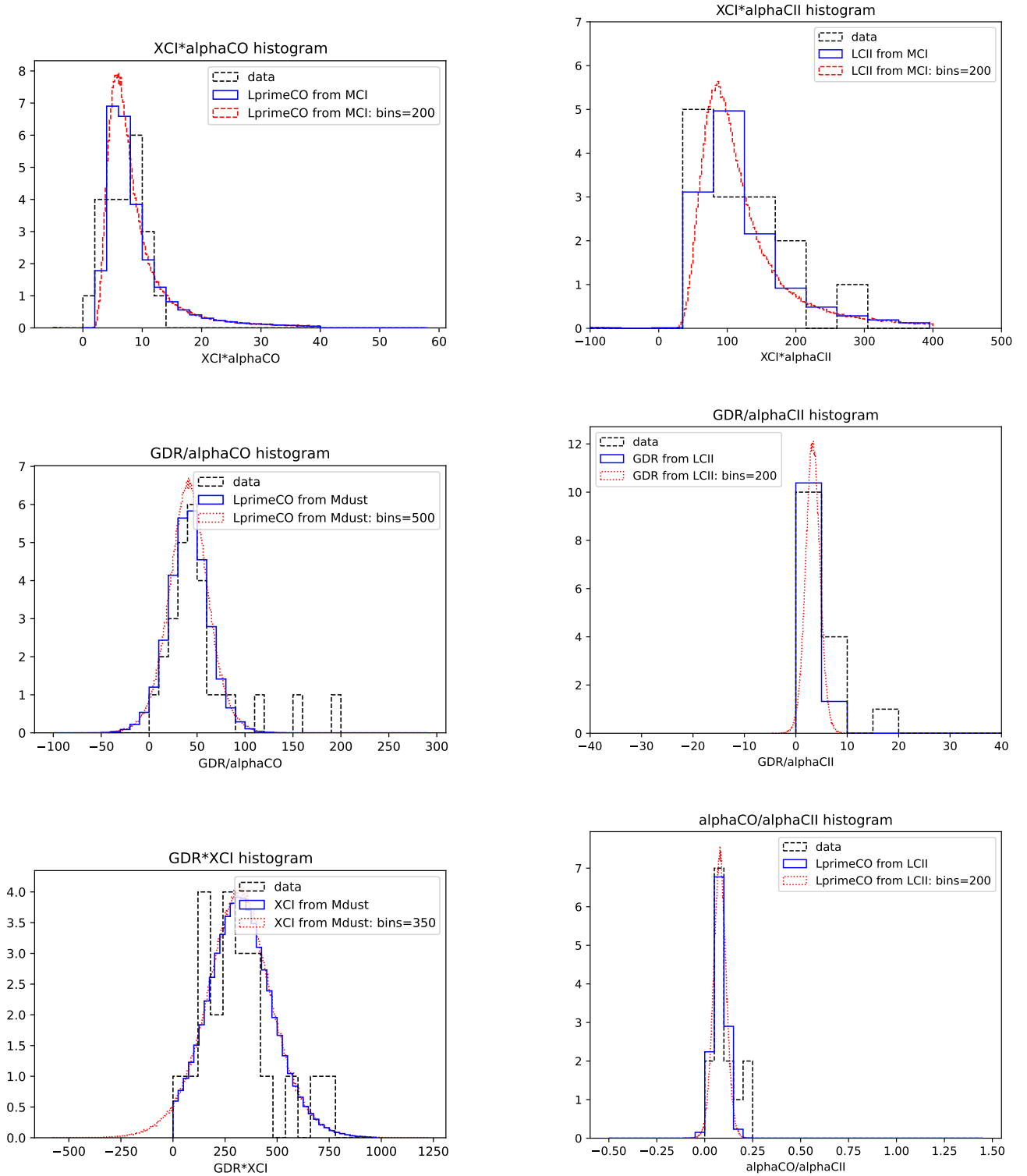


Fig. D.1. Cross-calibration with the tracers, $X_{\text{CI}} \times \alpha_{\text{CO}}$ (left) and $X_{\text{CI}} \times \alpha_{[\text{CII}]}$ (right), $\delta_{\text{GDR}}/\alpha_{\text{CO}}$ (left) and $\delta_{\text{GDR}}/\alpha_{[\text{CII}]}$ (right), and $X_{\text{CI}} \times \alpha_{\text{CO}}$ (left) and $\alpha_{\text{CO}}/\alpha_{[\text{CII}]}$ (right), are compared against the simulation described in Sect. D in the first, second, and third row, respectively. The resulting data, including the measurement uncertainty is represented as the blue solid line (binned the same as the original data), and the red dotted line.